Four-Dimensional Structure of Monthly Latent Heating Derived from SSM/I Satellite Measurements

SONG YANG AND ERIC A. SMITH

Department of Meteorology and Supercomputer Computations Research Institute, The Florida State University, Tallahassee, Florida

(Manuscript received 28 April 1997, in final form 19 March 1998)

ABSTRACT

Time–space distributions of mean monthly latent heating estimated from Special Sensor Microwave/Imager (SSM/I) passive microwave satellite measurements using the Florida State University precipitation profile retrieval algorithm over ocean regions are investigated for the 1992 annual cycle. The space domain is considered in both horizontal and vertical coordinates, with vertical retrieval made possible by the profiling design of the rain algorithm and the underlying relationship between the vertical derivatives of equivalent liquid water mass fluxes and latent heat release.

Comparisons of the retrieved mean monthly rainfall and rain frequency to climatological datasets and atoll rain gauge measurements indicate reasonable agreement except at latitudes above 40° where the satellite values are low biased relative to the climatologies. The horizontal distributions of mean monthly latent heating show that the locations of maximum heating lie in the vicinity and along the axes of well-documented large-scale convergence areas, particularly the intertropical convergence zone (ITCZ) and its transient offshoots, the South Pacific convergence zone (SPCZ), the tropical monsoon systems, and the middle-latitude storm tracks. The vertical distributions show that maximum heating rates of 5°C day^{-1} are located near the 5-km height level with positive heating extending to the top of the troposphere in the Tropics. Convection shifts associated with the 1992 El Niño–Southern Oscillation (ENSO) episode are well represented in the latent heating field. The seasonal variations of the ITCZ, SPCZ, and monsoon systems are clearly evident. The intraseasonal oscillation of latent heating during the northward propagation of the summer Indian monsoon is also a well-defined feature. Finally, the evolution of the Walker circulation is clearly depicted for both active and inactive ENSO conditions throughout 1992.

Emphasis is given to comparison and contrast of the SSM/I-derived heating fields to results given in the published literature. Many of the stationary and transient features appearing in the retrievals are consistent with previous studies concerning cloudiness, convection, and rainfall over low latitudes, with the exceptions stemming from specific features of the 1992 ENSO event. Therefore, the study provides a framework for using SSM/I measurements as a means to estimate the four-dimensional structure of latent heating over the tropical–subtropical oceans. Since the details of these structures are of considerable importance to the earth's weather–climate system both in terms of forcing and response, and by virtue of the design of a rain profiling algorithm, these results are presented as a necessary first step in seeking to use satellite measurements to obtain the most important component of the diabatic heating field.

1. Introduction

A thorough understanding of the atmospheric circulation is ultimately connected to an adequate knowledge of the time–space distribution of atmospheric heating. For example, Hartmann et al. (1984) have shown that the planetary-scale tropical circulation and the interaction between the Tropics and higher latitudes change substantially with different heating patterns. Also, a number of studies (e.g., Hack and Schubert 1990; Puri and Davidson 1992; Trenberth 1983) have demonstrated that in addition to the spatial distribution of heating, atmospheric circulations are sensitive to the vertical variation of the heating structure. Low-frequency oscillations in the Tropics, the foremost example of a tropical feature strongly affected by the vertical structure of heating, have possible connections to the El Niño–Southern Oscillation (ENSO), creating a link between intraseasonal and interseasonal timescales (e.g., Lau and Peng 1987). Thus, an accurate determination of the time–space variations of diabatic heating would be of substantial benefit to atmospheric prediction over a range of timescales.

Despite the importance of the four-dimensional structure of diabatic heating in governing atmospheric motion, there has been no direct measurement or dependable method of obtaining distribution of these profiles. It is particularly difficult over the ocean because of the lack of adequate conventional datasets. However, infra-

Corresponding author address: Prof. Eric A. Smith, Department of Meteorology, The Florida State University, Tallahassee, FL 32306-3034.
E-mail: esmith@metsat.met.fsu.edu

red (IR) and passive microwave (PMW) satellite measurements provide an alternative data source for estimating latent heating distributions. For example, rain rates retrieved from satellite and combined with surface observations are currently used to provide global monthly rainfall estimates for the Global Precipitation Climatology Project; see Arkin and Xie (1994) and Adler et al. (1994). These rainfall estimates are being applied to a number of research areas, such as climate diagnostic studies (e.g., Rasmusson and Arkin 1993; Schneider and Rudolf 1994), validation of rainfall forecasts from numerical weather prediction models (e.g., Janowiak 1992), and as input for surface process models (Shinoda and Lukas 1995). Moreover, rain rates retrieved from PMW satellite measurements and used for physical initialization have led to reduction of spinup time and improvement of precipitation forecast skill (Krishnamurti et al. 1993, 1994; Raymond et al. 1995). Also, PMW-retrieved rain rates used as input to a numerical prediction model for winter cyclones as latent heating functions have led to better cyclone forecasts in terms of intensity, track, and structure (Chang and Holt 1994).

A number of different algorithms are currently being utilized to retrieve precipitation over the oceans using IR and PMW datasets. The most physical approaches are the PMW algorithms (Wilheit et al. 1994; Smith et al. 1998). The Special Sensor Microwave/Imager (SSM/I) on board the Defense Military Satellite Program platforms have been used extensively for precipitation retrieval. The SSM/I measurements can provide information on vertical microphysical structure of the atmosphere because of their ability to penetrate deep within the cloud column (Smith et al. 1992a; Mugnai et al. 1993). For that reason, PMW measurements are generally more effective than IR measurements in retrieving quantitative information on instantaneous rain rates and latent heating profiles. The physically based inversion approach, such as developed at The Florida State University (FSU) and NASA/Goddard Space Flight Center (GSFC), which estimates vertical distributions of hydrometeors using SSM/I measurements (Smith et al. 1994a–c; Kummerow and Giglio 1994a,b; Kummerow et al. 1996), has advantages over the surface rain-rate-type algorithm because it can provide vertical profiles of both rain rate and latent heating (Yang and Smith 1998, manuscript submitted to *J. Appl. Meteor.*, hereafter YS; Yang and Smith 1999). In these two studies, latent heating rates were estimated by evaluating the vertical derivatives of retrieved liquid–ice water mass fluxes, which are proportional to latent heating. Tao et al. (1990, 1993) have also demonstrated with parameterized heating algorithms that the latent heating profiles of convective systems can be obtained by using liquid water content profiles retrieved with the FSU or GSFC algorithms (see Smith et al. 1992b).

A systematic measurement of the time–space distribution of latent heating from an independent source such as SSM/I measurements, or the more recent Tropical Rainfall Measuring Mission (TRMM) measurements [see Simpson et al. (1996) for an overview of the TRMM experiment], could help in resolving a number of discrepancies held over from research on global diabatic heating rates for cases and periods from the First GARP Global Experiment. Such discrepancies currently affect the understanding of recent global reanalysis products. For example, comparisons among results from Wei et al. (1983), Chen and Baker (1986), and Holopainen and Fortelius (1986) indicate differences in magnitude and spatial distribution due to differences in both the diagnostic methods and the analysis datasets and periods, although the distributions for large-scale systems are generally consistent. Yanai and Tomita (1998) have investigated the seasonal and interannual variations of the global distribution of apparent heat source (Q_1) and moisture sink (Q_2) terms calculated from a 15-yr National Centers for Environmental Prediction–National Center for Atmospheric Research reanalysis dataset. Their results show that both 4–5-yr and quasi-biennial oscillations of heat sources are evident over the equatorial central-eastern Pacific and equatorial Indian Ocean, respectively. However, recently discovered problems with the reanalyzed moisture products have raised questions about the magnitudes of the Q_2 results (M. Yanai 1997, personal communication).

Based on Tropical Ocean Global Atmosphere Coupled Ocean–Atmosphere Response Experiment (TOGA COARE) Intensive Flux Array (IFA) datasets, Yang and Smith (1999) showed that retrieved surface rain rates from SSM/I are consistent with rain rates obtained from the two TOGA COARE 5-cm shipboard radars in terms of rain rate magnitude, horizontal distribution, and temporal variation. They also evaluated the accuracy of latent heating profiles estimated from the vertical derivative mass flux approach, calibrated with a integral constraint scheme tied to surface rainfall from the shipboard radar measurements. Furthermore, they calculated $Q_1 - Q_2$ quantities from TOGA COARE soundings using the large-scale diagnostic approach of Yanai et al. (1973), demonstrating consistency between the retrieved latent heating profiles and the diagnosed Q_2 profiles. Yang and Smith (1998, manuscript submitted to *J. Appl. Meteor.*) then investigated the estimation of vertical eddy flux divergence of moisture from the residuals between the Q_2 profiles and the latent heat profiles for the IFA intensive operation period (IOP). Although the daily values of eddy moisture flux were noisy as a result of the residue approach, the noise was largely suppressed by use of a weekly filter. A comparison of the smoothed estimates of the vertical integrals of vertical eddy moisture flux divergence with independently measured surface evaporation over the IFA (equivalent terms) showed similar magnitudes and trends. The averaged values for 78 days were very close (within 6%) with a correlation coefficient of 0.57. These studies demonstrate that reliable latent heating rates can be retrieved from SSM/I measurements.

It stands to reason that retrieval of latent heating profiles from passive microwave measurements is met with uncertainties from various sources, plus the problem of the lack of dependable and accurate validation measurements. In general, uncertainty stems from latent heating being proportional to the vertical derivative of precipitation mass flux, which means that small errors in the slope of the rain-rate profile translate directly to errors in the latent heating. Notably, a principle scientific objective of the TRMM experiment is to understand the role of latent heating in driving the circulation of the global atmosphere. The main instruments for this purpose will be a PMW radiometer and a high-frequency (13.8 GHz) precipitation radar; see Simpson et al. (1996) for a description of the TRMM instruments. But in addition to the new measurements, there is a major emphasis on effective use of cloud models to help derive both the precipitation and latent heat profiles, in such a way to reduce the sensitivity of the diagnosed vertical heating structures to retrieval noise in the vertical rain structures.

Therefore, global distributions of latent heating retrieved from SSM/I measurements using a precipitation profile retrieval algorithm based on microphysics from precipitating cloud simulations can help establish a flame of reference for future TRMM datasets over the previous decade. The existing SSM/I archives provide a means to produce a short-term climatological record. This paper initiates that process by conducting a study of the space–time distribution of latent heating for a single year. We expect advances in our understanding of latent heating as more years are analyzed and as the TRMM measurements become available. The analysis is conducted over the 60°N–60°S ocean areas for the 1992 annual cycle in conjunction with the National Aeronautics and Space Administration's WetNet 3d Precipitation Intercomparison Project (PIP-3).

2. Methodology and datasets

The FSU precipitation profile retrieval algorithm is a physical inversion scheme designed to accept any combination of polarized or unpolarized satellite or aircraft PMW measurements. The algorithm uses a multispectral radiative inversion-optimization technique for a scattering media, designed to retrieve hydrometeor profiles of cloud and rain, along with precipitating and nonprecipitating ice profiles. The microphysical underpinnings for the algorithm are derived from the three-dimensional, nonhydrostatic, full physics cloud model of Tripoli (1992a,b). Latent heating profiles are calculated from the vertical mass flux profiles derived from the retrieved precipitating hydrometeor profiles. Two practical schemes for regional and global applications have been implemented for the algorithm. The second scheme is used in this study. An expanded algorithm description is given in the appendix.

The estimated latent heating due to the combination of ascending or descending cloud drops, raindrops, and graupel particles is given by the sum of the vertical derivatives of the mass fluxes:

$$Q(z) = \frac{g}{c_p}\left\{L_v\left[\frac{\partial R^*_{\rm cd}(z)}{\partial p}\right] + L_v\left[\frac{\partial R^*_{\rm rd}(z)}{\partial p}\right] + (L_v + L_f)\left[\frac{\partial R^*_{\rm ip}(z)}{\partial p}\right]\right\}, \quad (1)$$

where L_v/L_f are the latent heats of vaporization/fusion and c_p is isobaric specific heat.

The initial latent heating quantities are then adjusted according to a rain-rate category-based heating calibration scheme tied to C-band radar rainfall measurements from two research vessels positioned within the IFA during the TOGA COARE IOP. This calibration procedure is designed to create consistency between our retrieved heating profiles and those that are being obtained by other investigators from diagnostic $Q_1 - Q_2$ analyses using conventional data in which the TOGA COARE ship radars provide the vertically integrated latent heat fluxes for the heat and moisture budgets. The assumption behind the calibration scheme is that the vertical integral of retrieved latent heating must agree to an integral constraint provided by the radar-measured surface rainfall. The development of the method is described in detail by Yang and Smith (1999). The additive heating adjustment vector HA(z) valid for all z is given by

$$\mathrm{HA}(z) = \mathrm{Bias}_n(z)\left(1 + \frac{(\mathrm{RR}_s - \overline{\mathrm{RR}}_n)}{\mathrm{Scale}_n}\right) \quad n = 1, 2, \ldots, 5, \quad (2)$$

where z is the vertical coordinate, RR_s is the satellite retrieved rain rate, $\mathrm{Bias}_n(z)$ are the preassigned latent heating bias profiles for five categories of rain rates from the calibration analysis, $\overline{\mathrm{RR}}_n$ are the category averaged rain rates, and Scale_n are associated with the ranges of the category intervals as n changes from category 1 to 5. When RR_s is assigned to the appropriate rain rate category, the corresponding Bias_n vector, $\overline{\mathrm{RR}}_n$, and Scale_n used in Eq. (2) give the appropriate heating adjustment. Based on the analysis, the overall adjustment is only about 6% of an initially estimated value. This general discrepancy is below the prevailing uncertainties in either the conventional diagnostic methods or the more direct satellite rain mass flux methods in estimating latent heating, and thus calibration adjustment does not necessarily represent improvement to the initial estimates, but only a means to obtain consistency with diagnostic analyses.

The retrieval process is carried out pixel by pixel on SSM/I swaths over the 60°N–60°S oceanic areas for six alternating months during 1992 (January, March, May, July, September, November). The retrieved instantaneous rain-rate profiles are accumulated to monthly rainfall profiles at a 2.5° × 2.5° latitude–longitude grid res-

olution. Instantaneous latent heating rates are gridded on a daily basis to 5° × 5°, then calibration adjusted. Finally, the monthly mean latent heating rates are obtained by arithmetically averaging the calibrated daily heating rates over monthly time periods.

The general horizontal features of latent heating are analyzed using an approach in which the 3D heating field is first vertically integrated, then converted to a mean tropospheric heating rate so that the 3D heating structure is transferred to a 2D plane.

3. Space–time distribution of monthly rainfall

Before studying the distributions of monthly rainfall, we examine the sample populations of satellite pixels that go into the monthly averaging. The global distributions of monthly pixels over oceanic areas are analyzed for the six analysis months (figures not shown). Grids with monthly totals of more than 7000 pixels appear mostly over open ocean; coastal grids contain fewer pixels. May and July exhibit the largest areas exceeding 8000 pixels, with most of these areas found in the Southern Hemisphere oceans. In general, the Southern Hemisphere oceanic areas have more pixels than the Northern Hemisphere.

Since optimal daily coverage over a given area consists of four orbital swaths from two satellites, the maximum number of pixels for a month is about 8915 for a 2.5° lat × 2.5° long grid. Because the scan limits of an SSM/I instrument are not contiguous at low latitudes, total allowable pixels for most grids are less then this number, particularly as latitude decreases. Based on the above sample counts, the total pixels for most of 2.5° × 2.5° ocean grids exceed 78% of the optimal total pixel count per month. The smallest pixel percentages are ~50%, relative to the optimal count, and are found near coast lines. Therefore, although the frequency percentages are not uniform, the total sample populations that go into a given grid are large, denoting that statistical averaging will be reliable. However it should be noted, this excludes the possibility of persistent diurnal biases that a four times daily sampling design cannot detect.

a. General features

The monthly rainfall distributions for 1992 are shown in Fig. 1. All the well-documented large-scale features, such as the maximum rainfall axes along the ITCZ and South Pacific convergence zone (SPCZ), are evident. For January, one of the maximum precipitation areas, with a maximum value of more than 400 mm month^{-1}, is located in the west Pacific warm pool. Another one is found east of the date line at 5°N, 170°W. The third maximum is over the SPCZ at 25°S, 170°W. The nearly east–west-oriented rain belts due to storm tracks are obvious east of Japan and east of North America. Other relatively large rainfall areas are found southeast of Brazil and within the SPCZ. There are large precipitation totals over the north Indian Ocean, whereas the rainfall around the Indonesian region is relatively weak. By March, the maximum rainfall in the warm pool has shifted eastward to the date line, while the rainfall in the Indian Ocean migrates southward. Small rainfall totals

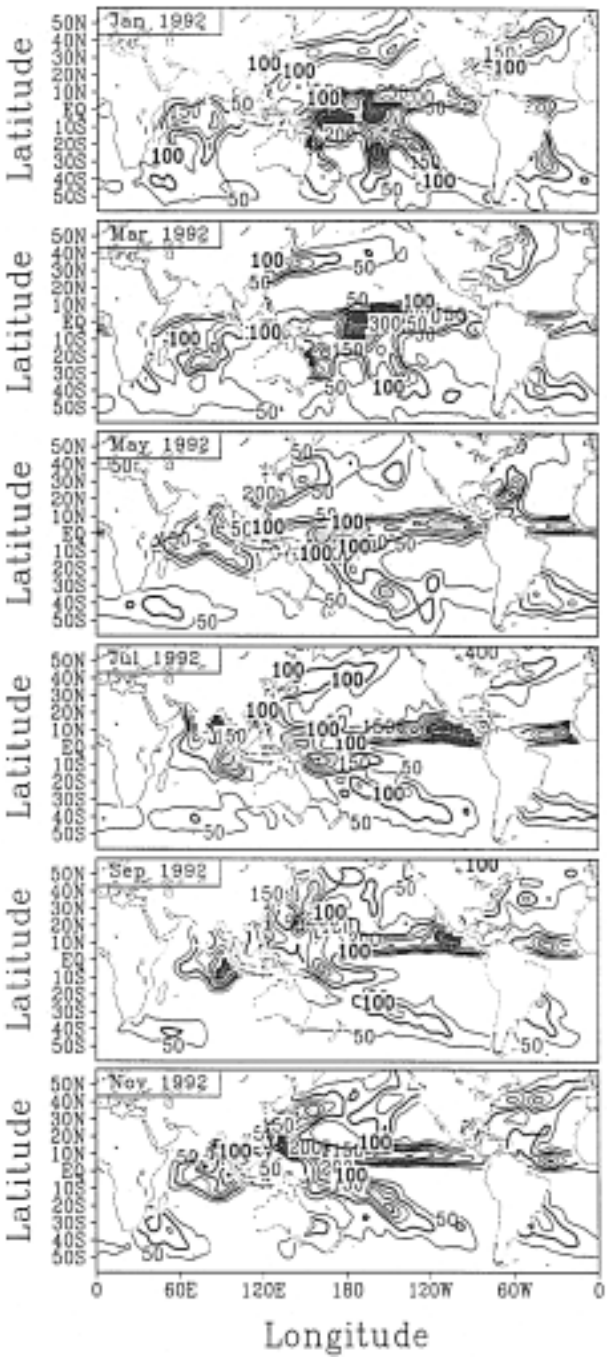

FIG. 1. Distribution of monthly rainfall over ocean for six alternating months during 1992. Contour interval is 50 mm month^{-1} up to 200 mm month^{-1}, after which shading is used with contour interval of 100 mm month^{-1}.

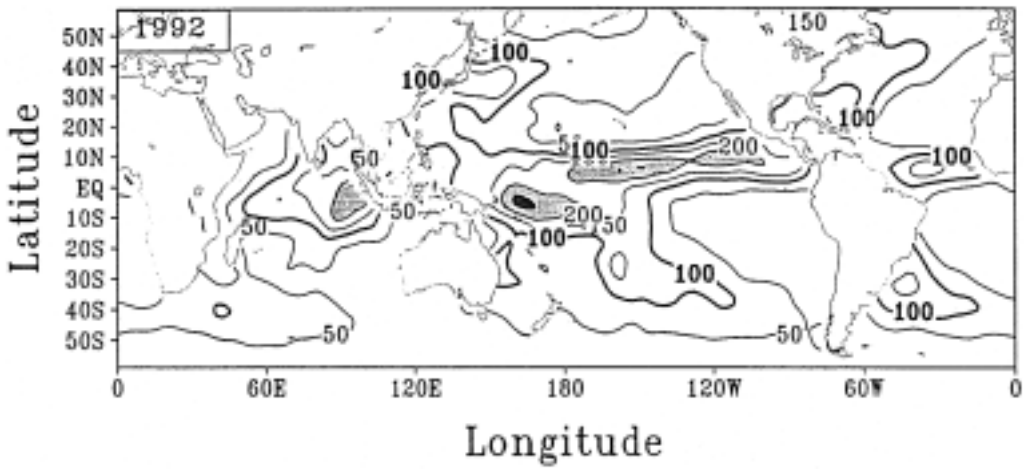

FIG. 2. Distribution of annual averaged rainfall over ocean. Contour interval is 50 mm month^{-1} with shading for rainfall more than 200 mm month^{-1}.

remain in the Indonesian region. From May to July, seasonal variation is apparent in the summer monsoon and evident in the northward migration of the ITCZ. Heavy rainfall begins to move northward into the Bay of Bengal in May, reaching its maximum in July. Rain in the South China Sea also increases during this period. These features correspond to development of both the summer Indian monsoon and east Asian monsoon. In the May–July period, precipitation in the central Pacific decreases while increasing in the Indonesian region. Maximum rainfall in the ITCZ shifts eastward to the east Pacific in July. Meanwhile, the SPCZ rainfall weakens. In September, the rainfall around the equatorial area of the Indian Ocean intensifies while the SPCZ further weakens. The intensification of precipitation over the regions of the Pacific Ocean is an indication of the effects on the extratropics by tropical weather systems. The ''V'' type of rain pattern over the Pacific Ocean is the dominant feature in November. The SPCZ gains strength again at its normal position. Rainfall over the central Pacific also intensifies while precipitation weakens over the Indonesian region.

The tropical atmospheric and oceanic indices and sea surface temperature anomalies (SSTAs) indicate that warm episode conditions intensified during June–August 1991 and reached a mature ENSO level by November 1991 (Janowiak 1993). The mature ENSO then intensified throughout December 1991–February 1992 (Kousky 1993) and persisted until the end of May 1992 (Wang 1993). During the ENSO intensification period, the SSTA and enhanced convection migrated eastward from the warm pool region of the west Pacific to the South America coast. During July–October 1992, convection returned to normal over the central and east-central equatorial Pacific while the positive SSTAs retreated westward to the date line (Mo and Wang 1994). By the following winter, another weak warm episode occurred again over the tropical Pacific Ocean. Ropelewski and Halpert (1987) showed that convective systems were suppressed over Indonesia, northern Australia, and the western half of the equatorial Pacific during the mature phase of ENSO. Thus, precipitation over these areas should be small during the 1991/92 ENSO period. The monthly rainfall distribution described above agrees with this result.

The rainfall variability, as described, is consistent with the pattern outlined by Rasmusson and Carpenter (1982), who described three major changes in the distribution of convection over the tropical Pacific during an ENSO event. The first one is the eastward shift of convection from Indonesia to the positive SSTA in the central and east-central Pacific. The second is the northeastward shift of the SPCZ. The third is the tendency of convection to shift equatorward from the normal ITCZ to the positive SSTA. The ITCZ and SPCZ distributions for the January rainfall distribution are consistent with Rasmusson and Carpenter's (1982) description, except that the eastern part of the ITCZ (east of 140°W) extends both northward and southward. This difference is also pointed out by Bell and Basist (1994) for the 1992/93 weak warm episode from an outgoing longwave radiation analysis. This would explain the differences in the rainfall pattern among various ENSOs.

Therefore, the features of our retrieved monthly rainfall reflect the distribution of SSTA, OLR, the large-scale circulation variation, and results from published ENSO studies. These provide confidence in the reliability of the retrieved global precipitation distributions based on the current version of the FSU SSM/I rain retrieval algorithm.

The annual average precipitation map is shown in Fig. 2. Large rainfall areas are clearly seen in the ITCZ, SPCZ, the northern Indian Ocean, and the storm tracks in the northern Pacific and Atlantic Oceans as well as the Brazil coast. The maxima of precipitation are located in the west Pacific warm pool area, the eastern part of

the Pacific ITCZ, and the Indonesian coast of the eastern Indian Ocean. Magnitudes of more than 250, 200, and 200 mm month^{-1} are associated with these three regions, respectively. All of these features are consistent with Spencer (1993) and Huffman et al. (1995) satellite analyses. However, the magnitudes are different. Spencer's results, based on a 14-yr Microwave Sounding Unit (MSU) data record, show that maximum rainfall is located in the eastern Pacific ITCZ area. The Huffman et al. estimates for July 1987–June 1988 were obtained from a combination of satellite estimates, rain gauge analysis, and numerical weather prediction model precipitation information. Their maximum annual rainfall was also located in the west Pacific warm pool area. Our estimates are more similar to Huffman et al. than to Spencer. The discrepancy may be due to interannual variations in precipitation as well as that our results involved only six months. However, further validation studies on precipitation retrieval are needed.

It is difficult to validate retrieved global distributions of monthly rainfall over oceans due to the lack of in situ measurements. However, indirect assessments using climatological datasets can qualitatively verify the credibility of retrieved monthly rainfall. Two categories of monthly rain coverage and rainfall will be examined here. Climatological rain frequency maps over oceans were published by Petty (1995) based on the shipboard present-weather reports from the Comprehensive Ocean–Atmosphere Data Sets (COADS). Also, two sets of climatological monthly rainfall over oceans from ship reports were published by Legates and Wilmott (1990) and Jaeger (1983).

Figure 3 is the distribution of monthly raining pixel percentage from SSM/I retrievals, which reflects the rain frequency distribution. It is not surprising that the rain frequency distribution is similar to that of monthly rainfall. The most frequent raining areas are the ITCZ, SPCZ, summer Indian monsoon system, and the storm tracks. The monthly rain frequency is greater than 10% with a maximum of approximately 25% in the central Pacific ITCZ during the Northern Hemisphere winter, and about 10% with a maximum of 15% in the SPCZ. The summer Indian monsoon area also exhibits more than 10% rain frequency with a maximum of more than 20% in July. The magnitude and distribution of rain frequency in the Tropics and subtropics are similar to the Petty (1995) results. However, large differences exist in the high latitudes, in which Petty's results show relatively high magnitudes while our results indicate low values. There are three possible reasons for this discrepancy. First, there were fewer ship reports used in Petty's analysis in the higher latitudes, which could lead to greater uncertainties. Second, the rain screening scheme we are using may have limitations at high latitudes, failing to detect many raining pixels with small rain rates, resulting in lower rain frequencies. The third and most likely reason is that the FSU precipitation algorithm does not effectively detect precipitating snow without melting conditions. This would lead to part of the total rainfall in the higher latitudes being missed.

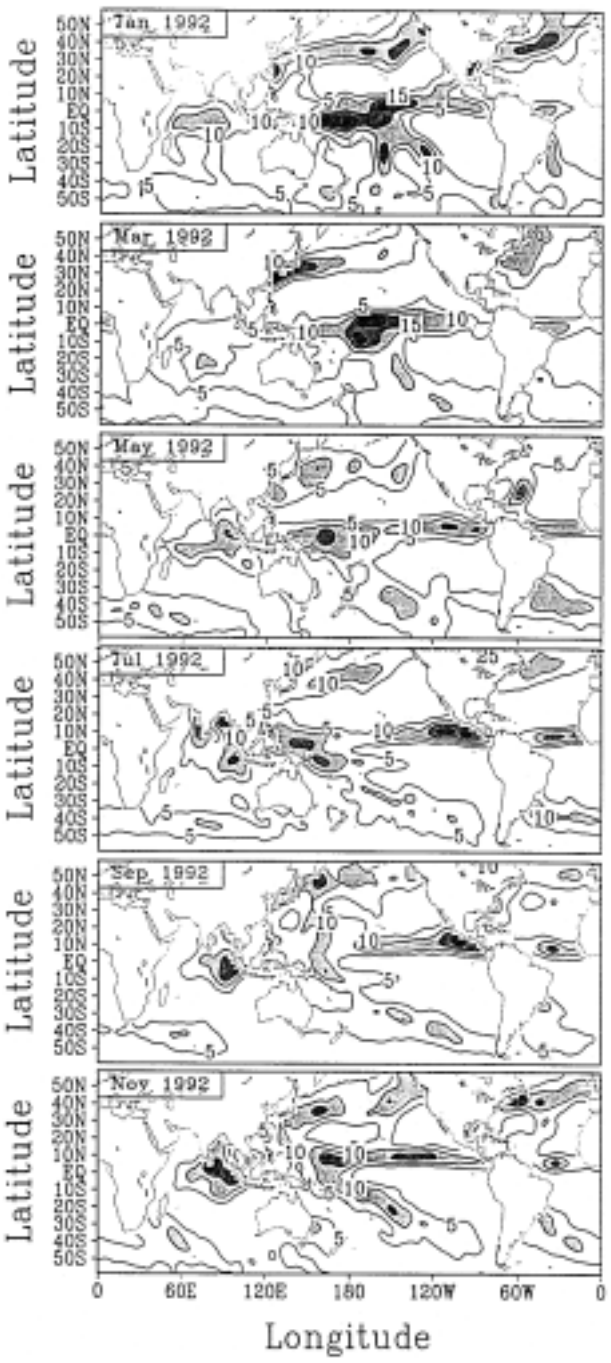

FIG. 3. Distribution of monthly raining SSM/I pixel coverage over ocean for six alternating months during, 1992. Contour interval is 5% with shading for coverage more than 10%.

Comparing the distributions of monthly rainfall and rain frequency, the main difference is in identifying the SPCZ. The SPCZ is clearly seen throughout the year from the monthly rainfall maps, with maximum strength during the Northern Hemisphere winter. However, its

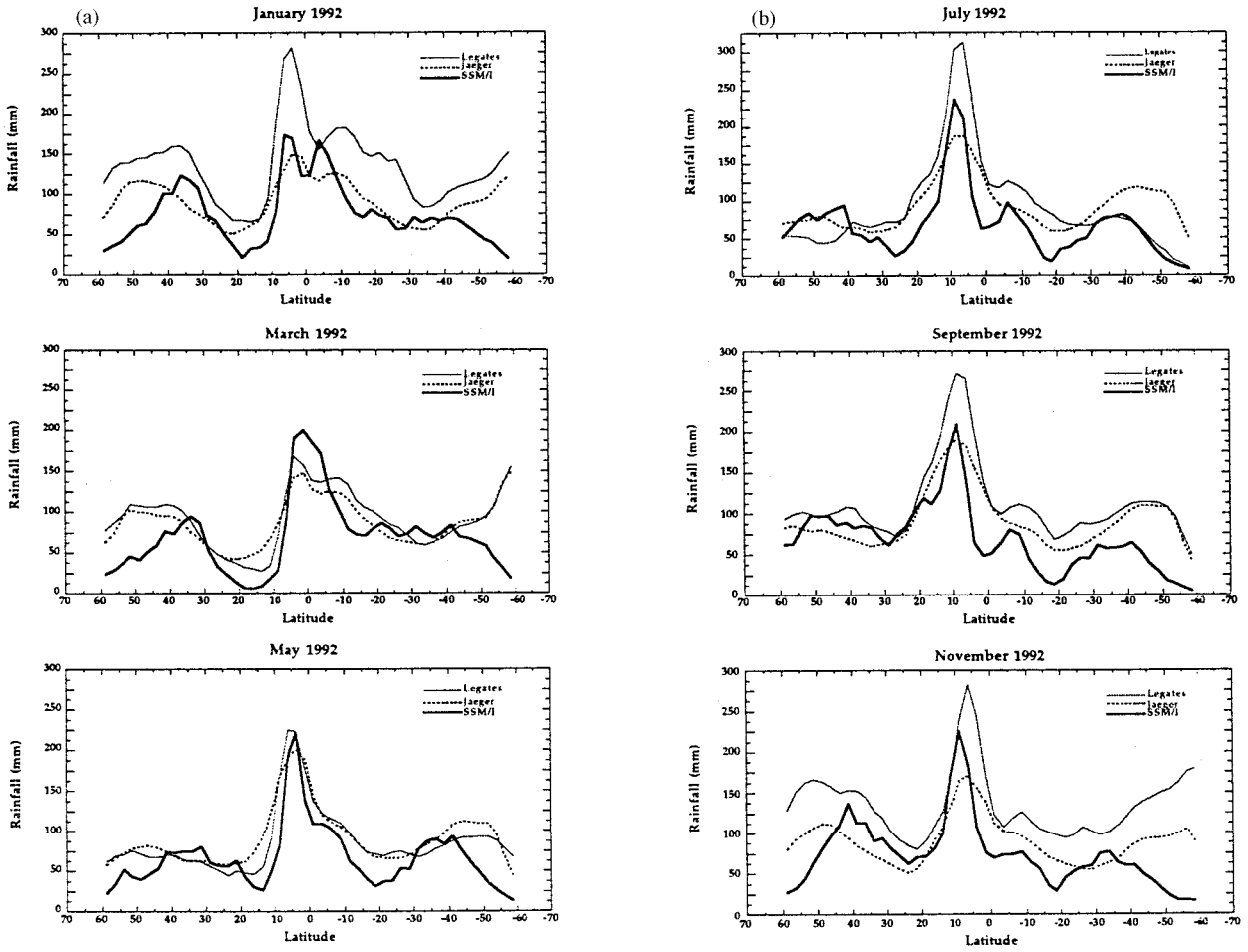

FIG. 4. (a) Comparison of zonal mean monthly rainfall over 60°N–60°S oceanic region between SSM/I and climatological datasets for January, March, and May 1992. (b) Same as (a) except for July, September, and November 1992.

position is not as obvious in the rain frequency distribution maps except for the Northern Hemisphere winter. This suggests that the disturbances in the SPCZ are transient waves.

Two areas of caution are advised in the comparison of retrieved monthly rainfall and climatological data. Since the climatological monthly rainfall totals do not correspond to the satellite estimates for the comparison year, the intercomparisons can only be used for detecting obvious biases in the magnitude and location of the rainfall. Second, climatological data in some ocean areas have very low confidence because of the scarcity of observations. Thus, only zonal mean monthly rainfall will be examined.

Figures 4a,b present the zonal averaged distributions of the two climatological datasets and the satellite retrievals for the six alternative months of 1992. It is obvious that the two climatological datasets in March and May are similar; they are also similar in July and September except for a higher value in the ITCZ for the Legates and Wilmott data. On the other hand, the magnitudes are much larger in the Legates and Wilmott dataset during January and November. The general shapes of the three distributions are roughly the same, except for the drier subtropics in the winter hemispheres from the retrieved results. This dry bias may result from the rainfall screen failing to detect light rain rates or it may be a specific characteristic of 1992. The retrieved ITCZ is also narrower than found in the climatological data. The retrieved rainfall in the ITCZ during January, July, September, and November is less than the Legates and Wilmott data but greater than Jaeger. There is a maximum center located at the ITCZ near 140°W in the horizontal distribution of annual rainfall from the Legates and Wilmott data. This maximum value would lead to the larger zonal mean of Legates and Wilmott data in Fig. 4. This feature did not appear in the Petty (1995) and Huffman et al. (1995) analyses. Spencer (1993) also noted that this feature was not consistent with his 14-yr retrieved rainfall climatology based on MSU measurements. He explained that the extreme annual rainfall in the Legates and Wilmott (1990) analysis was uncharacteristic and due to the scarceness of ship data in that area. The major difference between the re-

trieved and climatological monthly rainfall is in the region above 40° latitude, where the retrieved values have a low bias, probably for reasons discussed above.

The correlation coefficients of retrieved zonal monthly rainfall to climatological data are greater than 0.45 with a maximum of 0.82, all at the 1% level of significance. For small regions, the retrieved monthly rainfall was compared to atoll rain gauge measurements from PIP-3 summary reports (Adler et al. 1996). The overall bias, ratio, rms, and correlation coefficient for the six months are −63.3 (mm), 0.73, 121.5 (mm), and 0.72, respectively. The underestimation is common feature among the PIP-3 algorithms. These statistics are consistent with others.

b. Space–time propagation

The temporal variations of large-scale rain systems are shown by Hovmöller-type diagrams. The temporal variation of zonal mean monthly precipitation is depicted in Fig. 5 (top). The prominent feature in this figure is the maximum rainfall axis located at tropical latitudes, with the maximum located in the equatorial area in January, then slowly migrating northward until July–August. The northward progress accelerates in March. This rapid movement stops in July when the maximum rainfall is at 5°N. The maximum rainfall remains at that position in the following months. Another rainfall maximum region at extratropical latitudes during the Northern Hemisphere winter reflects the storm tracks.

The temporal variation of averaged monthly tropical rainfall (over 5°S–5°N) is shown in Fig. 5 (bottom). From January to April, the largest precipitation areas, with maxima of more than 350 mm month^{-1}, remain in the central and central-east Pacific with a slight extension eastward. Two secondary maxima during this period are in the Atlantic and Indian Oceans. The maximum rainfall in the central Pacific then moves westward until July when it reaches the west Pacific region. During this period rainfall in the Indian Ocean intensifies. After July, maximum rainfall in the Pacific migrates eastward and arrives at the date line in November. These temporal changes of maximum rainfall in the Pacific Ocean are consistent with the SSTA variations described above so that the space–time distribution of precipitation clearly depicts the 1992 ENSO episode.

Three important weather–climate system regions are selected to investigate the meridional propagation of monthly precipitation. The summer Indian monsoon region is defined as the area of 0°–30°N, 75°–95°E. Figure 6 shows the time–latitude sections of monthly rainfall over the summer Indian monsoon (top), the west Pacific warm pool (middle), and the east Pacific region (bottom). During the 1992 ENSO warm episode, the maximum precipitation area is found at 5°S over the monsoon region with small rainfall totals in the northern part of the Indian Ocean. In the warm pool area, the maximum rainfall is also at 5°S. The relatively large rainfall accumulations at 20°S and 35°N are due to the SPCZ and storm tracks. The maximum precipitation area in the east Pacific lies at 5°N. During the summer and fall, the main rainfall in the monsoon region shifts to 20°N, which clearly shows the results of monsoon circulations. Rainfall in the warm pool area slowly extends northward and arrives at 5°N in November. The maximum precipitation area had remained around 10°N since July over the east Pacific, indicating persistent rain systems.

4. Space–time distribution of monthly mean latent heating

a. Horizontal distribution

Figure 7 shows the evolution of vertically averaged monthly mean latent heating during 1992. In January, maximum heating rates of 1.75° and 1.5°C day^{-1} are located in the west Pacific warm pool and the central-east Pacific, respectively. A second primary heating center is in the tropical region of the Indian Ocean. The broad area of large heating in the southern tropical area of the Pacific Ocean reflects the northeast extension of the SPCZ, representing the effect of the 1992 ENSO episode. Heating moves east of the international date line during January–March, while heating in the Indian Ocean decreases. Heating continued to shift to the South America coast, with maximum values retreating westward to the warm pool region from March to May. The heating in the equatorial area of the Indian Ocean intensifies during this period. In July, the maximum heating moves northward to the Asian and central American coasts, as well as the Bay of Bengal. From July to September, the heating in the west Pacific and the Bay of Bengal decrease during the withdrawal of the summer Asian monsoon. In November, maximum heating is located in the west Pacific warm pool and the tropical area of the Indian Ocean. The V-type heating pattern in the Pacific is its most important feature, and consistent with published results (e.g., Vincent 1994). Relatively large heating rates are found in the SPCZ area each month but peak intensities are reached during the Northern Hemispheric winter.

The vertically annually averaged latent heating is shown in Fig. 8, indicating large heating rates in the ITCZ, SPCZ, monsoon region, and storm tracks. The largest heating rates are located in the west Pacific warm pool and near Indonesian in the Indian Ocean. A maximum heating rate of 1.5°C day^{-1} is found in the warm pool area.

Based on the TOGA COARE analysis, maximum heating of Q_1 and Q_2 is around 5 km, which is close to the model layer of 4.2–5.0 km. The monthly distributions of heating rates in this layer are well correlated to the total vertically averaged heating rates (not shown). In general, heating rates greater than 2.0°C day^{-1} are

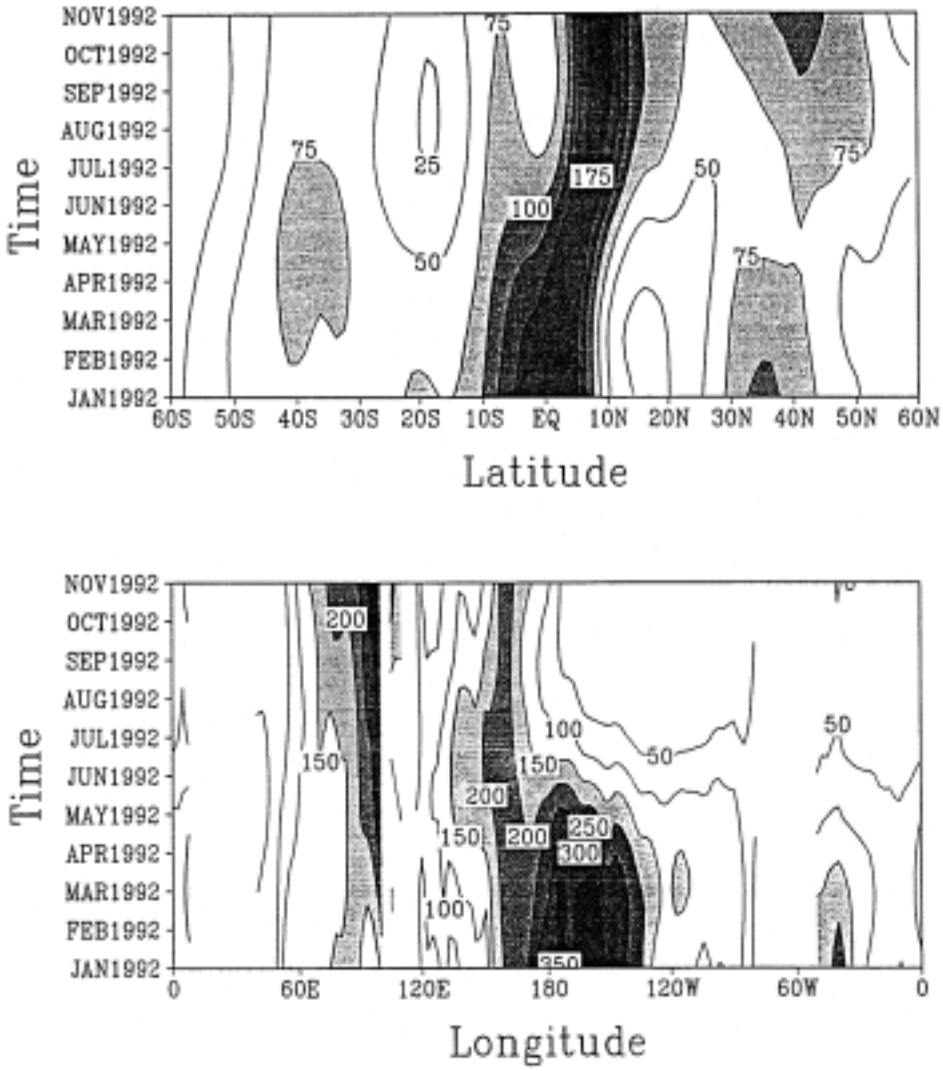

FIG. 5. Time–latitude section of zonally averaged (top) monthly rainfall and (bottom) time–longitude section of meridionally averaged (5°S–5°N) monthly rainfall over ocean. Contour intervals are 25 (50) mm, with shading for rainfall greater than 100 (150) mm, respectively.

mainly located in the ITCZ, SPCZ, and the summer monsoon region. Heating in the Atlantic ITCZ area is relatively small, which is consistent with the fact that it is not as active as the ITCZs of the Pacific and Indian Oceans. Maximum amplitudes reach 6.0°C day^{-1} in the Pacific ITCZ region, including the IFA area. This magnitude is similar to that found for Q_2 estimates from YS and the total heating over equatorial western Pacific from the results of Schaack et al. (1990).

b. Space–time propagation

Figure 9 (top) shows the temporal variation of zonally and vertically averaged monthly mean latent heating. Maximum heating rates lie in the equatorial areas from January to May, then shift to 10°N in September, and withdraw to 5°N in November. These movements describe the main north–south propagation of the heating field during an annual cycle. Figure 9 (bottom) describes the east–west propagation of latent heating in the deep Tropics (5°S–5°N). It is obvious that the dominant heating region is located in the Pacific with a maximum of 1.75°C day^{-1}. Another large heating region is found in the Indian Ocean. From January to May, maximum heating in the central Pacific Ocean extends to the eastern Pacific. The maximum heating regime starts to propagate westward in March reaching the western Pacific in July. Then it slowly returns to its normal position over the warm pool area by November. This kind of temporal variation of latent heating is consistent with the propagation of SSTAs in the Pacific (Wang 1993; Mo and Wang 1994), which reflects the evolution of the 1992 ENSO event.

The detailed north–south propagation of the heating

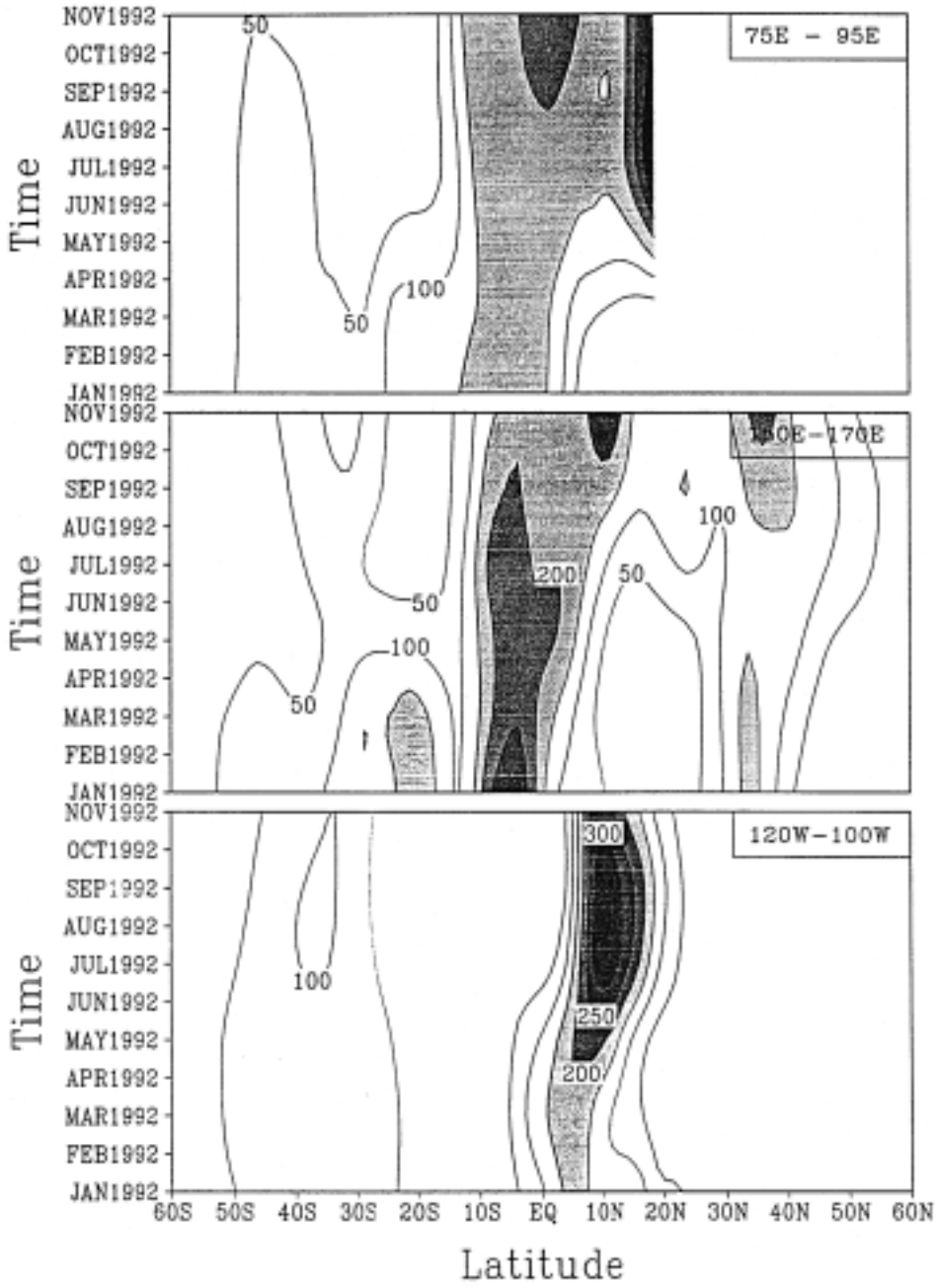

FIG. 6. (top) Time–latitude sections of averaged monthly rainfall over selected ocean regions: summer Indian monsoon (top), west Pacific Ocean (middle), and east Pacific Ocean (bottom). Contour interval is 50 mm with shading for rainfall more than 150 mm.

field is given in Fig. 10 for three selected weather–climate regions, which include the summer Indian monsoon (top), the west Pacific warm pool Fig. 10 (middle), and the east Pacific Fig. 10 (bottom). Areas with large heating rates for the monsoon region are found along the equator always, with maxima of 1.25°, 1.25°, and 1.5°C day^{-1} in January, May, and November, respectively. Another significant feature of the monsoon area is the northward movement of large heating rates in summer, corresponding to the summer Indian monsoon circulation. A maximum heating rate of 1.5°C day^{-1} is found at 20°N in July. In addition, there are two separate maximum heating centers located at 5°N in May and 20°N in July during the northward migration of the major heating regime. This indicates a low-frequency oscillation in the heating field during the development of the summer Indian monsoon. Therefore, three interesting features are captured in the heating field over the

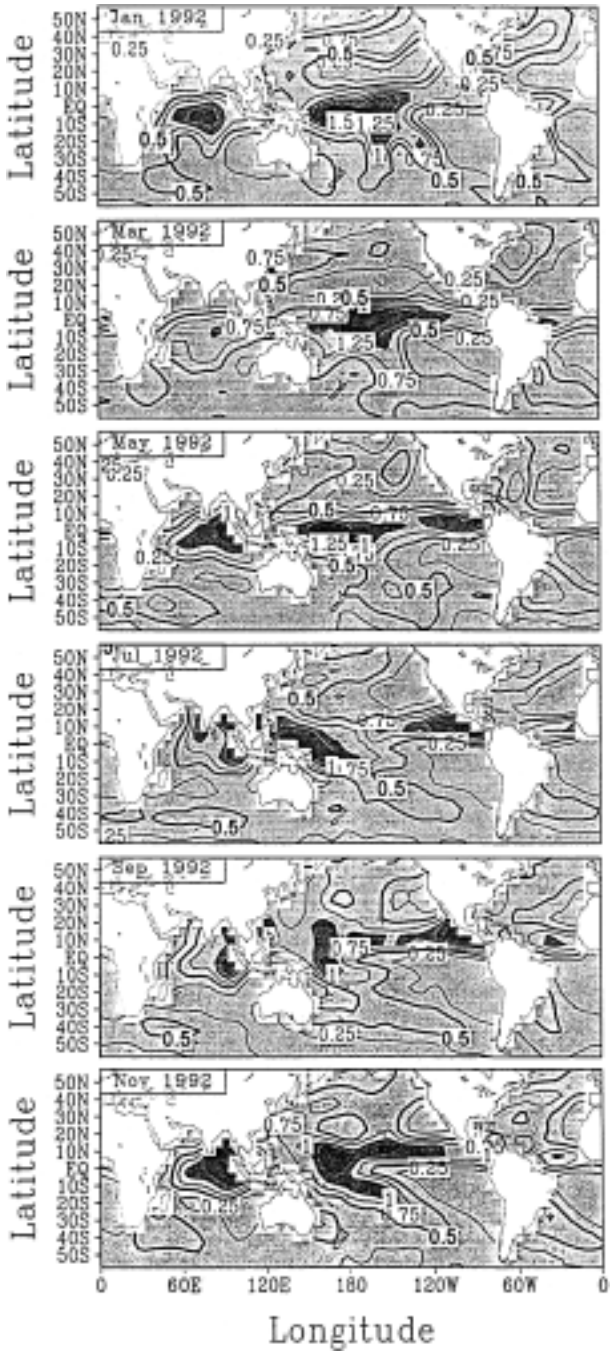

FIG. 7. Horizontal distribution of vertically averaged monthly mean latent heating over ocean for six alternating months during 1992. Light shaded areas indicate data coverage. Contour interval is 0.25°C day^{-1} with heavy shading for heating more than 1.0°C day^{-1} (bold line is 0.5°C day^{-1}).

monsoon area: 1) seasonal variation of the latent heating in equatorial areas with maximum heating in winter and summer, 2) northward migration of latent heating in summer associated with the evolution of the monsoon circulation, and 3) intraseasonal oscillations of latent heating during its northward propagation. All of these features have been well documented (e.g., Yasunari 1979; Sikka and Gadgil 1980; Lau and Chen 1985).

Over the west Pacific warm pool area, maximum heating is found around the equator with a maximum of 1.5°C day^{-1} at 5°S in January and July. In addition, the largest heating rates start to extend northward in March, reaching 20°N in September. There is maximum heating of 1.5°C day^{-1} located around 5°N in May as the heating is shifting northward. Thus, the seasonal variation of latent heating and its slow extension northward from winter to summer are obvious. Due to the effect of the 1992 ENSO episode, the maximum heating at 10°N in the east Pacific shifts to the equatorial area from January to March. After that, the maximum heating area migrates northward to 10°N in September with a maximum of 1.75°C day^{-1} in the summer. The maximum heating withdraws to the equator from September to November. This variation of heating suggests only an annual oscillation in the east Pacific area, demonstrating that the semiperiodic characteristics of diabatic heating change from region to region.

c. *Vertical distribution*

The large-scale circulations in the Tropics are responding to the pattern of diabatic heating, which exhibits a strong departure from zonal symmetry. The zonal circulations along the equator have several cells in which the Pacific Ocean Walker circulation is dominant in both scale and amplitude. Webster (1983) and Webster and Chang (1988) discussed how the rising branch of the Walker circulation is located in the west Pacific during normal conditions, with the circulation shifting in position (and upward motion) to the central and central-east Pacific region during an El Niño period. In their studies, 3D structures of diabatic heating associated with these circulations were not available. With the retrieved latent heating from SSM/I measurements, we are able to explore the heating evolution during the 1992 ENSO period.

Figure 11 shows the height–longitude sections of monthly mean latent heating over 5°S–5°N for the six analysis months. The most prominent vertical features are a heating rate maximum of 5.0°C day^{-1} peaking around 5 km, and a secondary peak at 1 km. During the 1992 ENSO warm episode (January–March), areas of large heating cover the entire Pacific with maxima in the central Pacific. The heating extends to the top of the troposphere. Heating rates in the Indian and Atlantic Oceans are relatively small. These heating distributions describe the anomaly heating structures for the 1992 ENSO episode. The heating shifts westward with decreased intensity over the Pacific in May (the decay period of the 1992 ENSO), while heating in the Indian Ocean increases. The maximum heating regime moves to the west Pacific, while small heating rates are found in the east Pacific during the normal conditions of July, September, and November. Central and South American

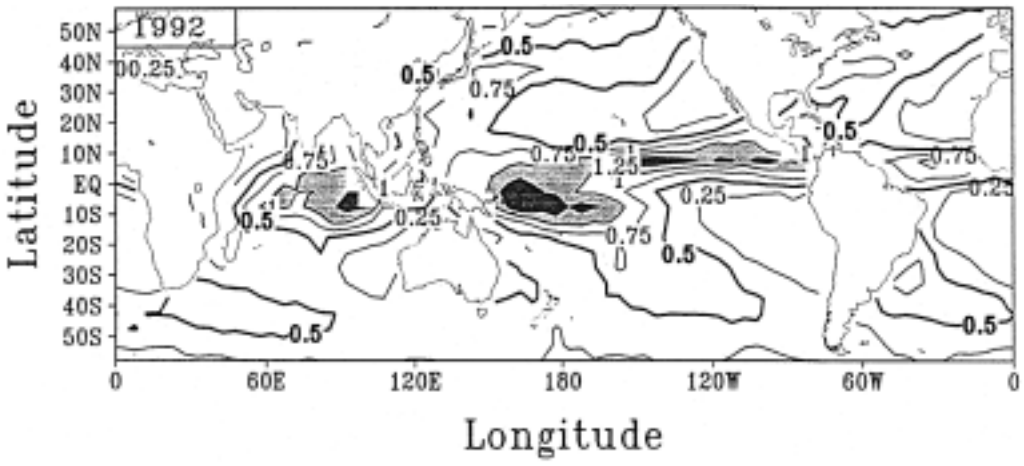

FIG. 8. Distribution of annual average latent heating over ocean. Contour interval is 0.25°C day^{-1} with shading for heating more than 1.0°C day^{-1} (bold line is 0.5°C day^{-1}).

areas develop into additional heat sources during this period. These heating distributions clearly depict the Walker circulation under normal conditions. Therefore, the vertical latent heating structures over the equatorial area show the Walker circulation evolution during normal and ENSO conditions, which are consistent with previous studies (Webster 1983; Webster and Chang 1988).

The height–latitude sections of monthly mean latent heating over the selected weather–climate system areas for the six analysis months are also studied (not shown). The general features are that the maximum heating is located in the Tropics with additional maxima in the extratropical regions of the Southern and Northern Hemispheres. Maximum heating is around 5 km with a secondary peak near 1 km. The differences in heating structures between the Tropics and extratropics are obvious. The heating in the Tropics can extend to the top of the troposphere while the heating in the extratropics only reaches about 8 km. It should be pointed out that the vertical structure of latent heating at latitudes higher than 40° may not be completely valid because the deposition effects due to snow formation are likely underrepresented in the total latent heat release profile.

The northward migration of heating over the monsoon region is significant during the summer period while the north–south movement of heating over the warm pool area is not as clear. The maximum heating over the east Pacific remains at 10°N in January, moving to equatorial areas in March due to the 1992 ENSO. Then it moves back to 10°N in July, persisting there until November.

d. Quasiperiodic behavior over SPCZ

The analysis in section 4b confirmed that latent heating has periodic oscillations at intraseasonal, seasonal, and possibly annual timescales. The SPCZ, as represented by its latent heating features, is much stronger in amplitude in the Northern Hemispheric winter than at any other time. Vincent (1994) provides a review of the broad scope of the SPCZ, consisting of a zonal portion, located in the west Pacific warm pool region, and a diagonal portion, oriented northwest–southeast. One of the important features of the SPCZ is its quasiperiodic behavior. Its seasonal oscillation is addressed here.

As shown in Fig. 7, the zonal portion of the SPCZ is located around the date line, where it merges with the ITCZ. The diagonal portion extends to 40°S, 130°W. Figure 12 depicts the characteristics of latent heating at the date line, 150°W, and 175°E–135°W. From January to July, a single maximum persists around 5°S at 180°, which indicates merging of the ITCZ and the zonal portion of the SPCZ. In September and November, two separate maxima show the positions of the SPCZ and ITCZ. From January to March at 150°W, the large heating area extending to 30°S clearly indicates the diagonal portion of the SPCZ while the maximum is still around the equator. The less than obvious separation between the SPCZ and ITCZ from January to March reflects that the diagonal portion extends northeastward due to ENSO effects discussed in Fig. 9 and Rasmusson and Carpenter (1982). The diagonal portion is not distinct until November when two separate maxima in the heating field clearly differentiate the ITCZ and SPCZ. The averaged heating over the SPCZ (bottom panel) shows the features combined from the top and middle panels. The SPCZ is more active in the Northern Hemisphere winter. The response of latent heating over the SPCZ to the 1992 ENSO episode is consistent with results from Rasmusson and Carpenter (1982) and Meehl (1987).

The departures of vertically averaged monthly latent heating from the annual average (Fig. 13) mimics the patterns in Fig. 12, however with more clarification of the seasonal evolution of the SPCZ. During summer, negative values imply a weak SPCZ. Even the ITCZ is

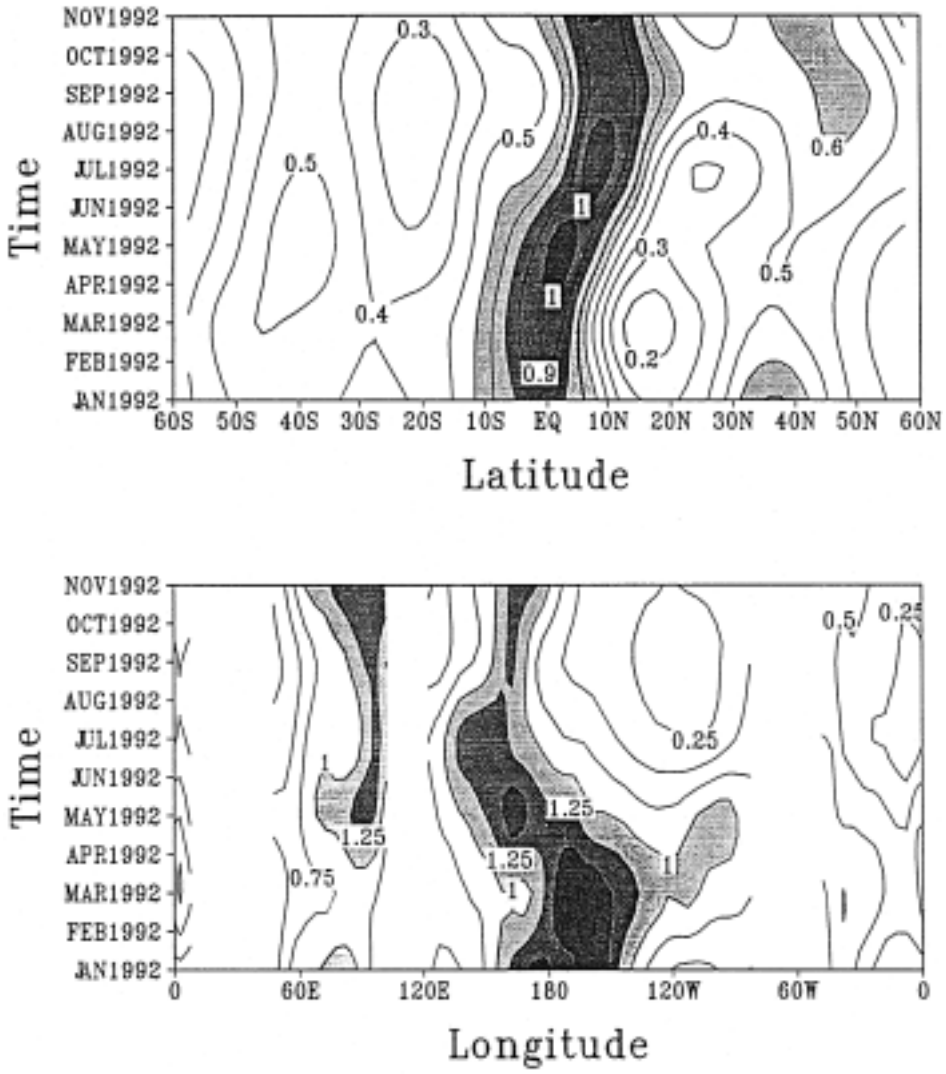

FIG. 9. (top) Time–latitude section of vertically zonally averaged monthly latent heating and (bottom) time–longitude section of vertically meridionally (5°S–5°N) averaged monthly latent heating over ocean. Contour intervals are 0.1°C (0.25°C) day^{-1} with shading for heating more than 0.6°C (1.0°C) day^{-1}, respectively.

weak over the SPCZ longitude corridor. Separate maxima in the middle panel show the SPCZ–ITCZ systems in January and November.

The similar departure of vertically averaged monthly mean latent heating from the equator to 15°S is shown in Fig. 14 in order to examine the periodic behavior of the SPCZ and its connection to the Indian and west Pacific Oceans. Several interesting features are observed in this diagram. The heating departures in the Indian Ocean, west Pacific, and east Pacific are in phase, while the departure in the SPCZ (central-east Pacific) is out of phase. The out-of-phase relationship between the Indian and Pacific Oceans is due to the eastward propagation of disturbances. It is apparent that disturbances intensify once they appear in the eastern Indian Ocean, central Pacific, and eastern Pacific during their eastward propagation. The disturbances move slowly from January to April, then faster from April to May. They then remain stationary during June to September, shifting eastward rapidly from September to November. The fast eastward propagation occurs only in the transition period between seasons, underscoring the seasonal variability of the disturbances. In addition, intraseasonal variations appear during the slow eastward propagation of the disturbances. However, these features cannot be investigated in detail with monthly mean datasets.

5. Discussion and conclusions

Time–space distributions of monthly mean latent heating, derived from SSM/I measurements in conjunction with the physically based FSU PMW rain-profile retrieval

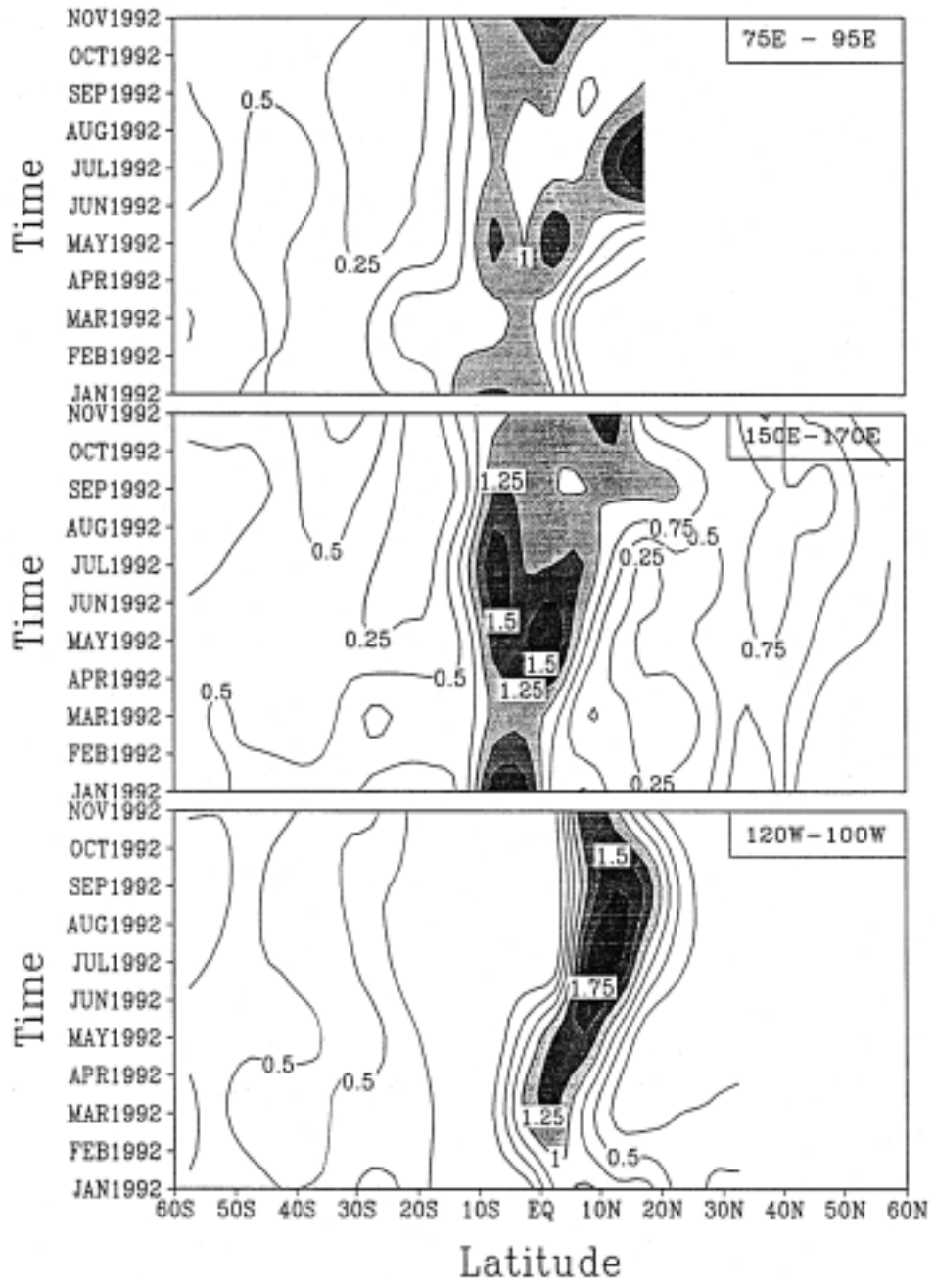

FIG. 10. Time–latitude section of vertically averaged latent heating over selected ocean regions: summer Indian monsoon (top), west Pacific Ocean (middle), and east Pacific Ocean (bottom). Contour interval is 0.25°C day^{-1} with shading for heating more than 1.0°C day^{-1}.

algorithm, have been used to depict the main diabatic heating features embedded in the global circulation. The retrieval scheme is applied to the 60°N–60°S ocean areas for the 1992 annual cycle based on alternating months (January, March, May, July, September, November). Since it is not straightforward to directly validate the global latent heating field, we have made use of the existing literature in assessing the heating structure, as well as performing climatologically based validation on the precipitation retrievals underlying the latent heating estimates. For the precipitation algorithm, we have assumed that a three-dimensional nonhydrostatic cloud model can provide the microphysical underpinnings for an inversion-based retrieval procedure. We also assume that the vertical derivative of the precipitation mass flux is proportional to latent heating released from condensation and/or deposition processes.

The distributions of monthly rainfall and rain fre-

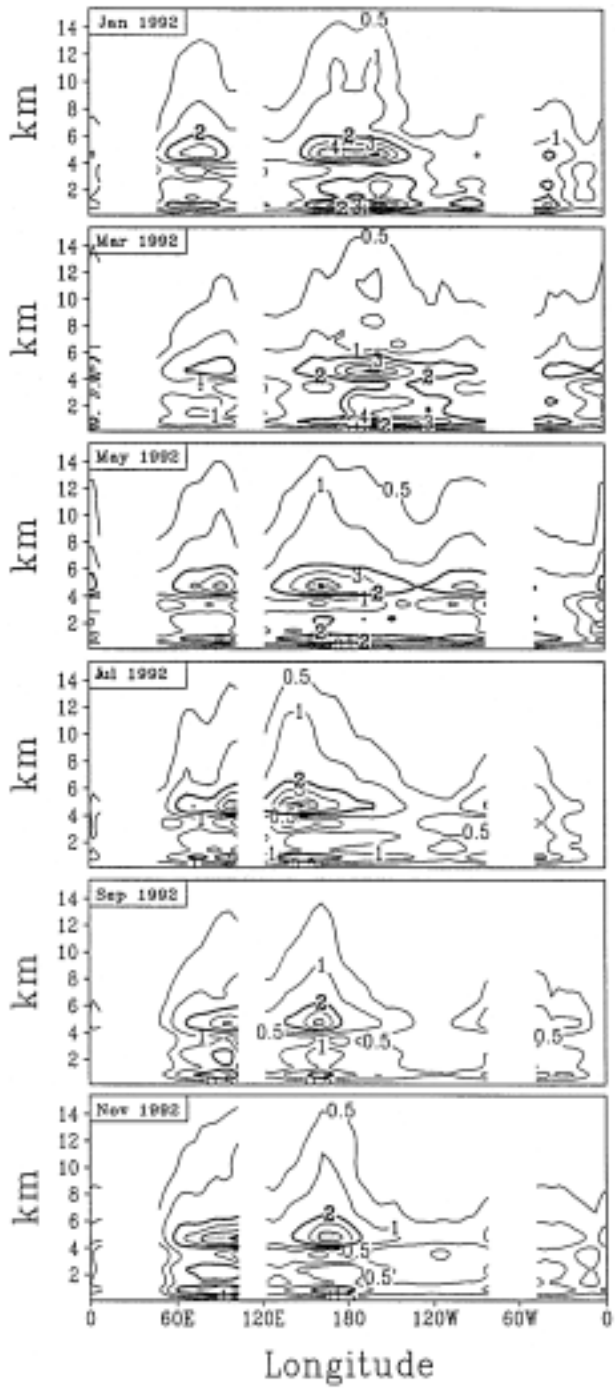

FIG. 11. Height–longitude sections of monthly latent heating over 5°S–5°N ocean area for six alternating months during 1992. Blanked out contour regions indicate land areas. Contour interval is 1.0°C day^{-1} (except for first contour which is 0.5°C day^{-1}) with shading for heating more than 4.0°C day^{-1} (bold line is 2.0°C day^{-1}).

quency demonstrate that the maximum rainfall and rain frequency centers are well associated with large-scale circulation systems, particularly the ITCZ, SPCZ, the Asian monsoon, and midlatitude storm tracks. Maximum monthly rainfall of more than 400 mm month^{-1} and a rain frequency of approximately 25% were found in the central Pacific ITCZ during the Northern Hemisphere winter. For intercomparison, climatological rain frequency distributions from shipboard weather reports were obtained from the COADS dataset. These intercomparisons indicate similarities with magnitudes comparable in both the Tropics and subtropics, although the retrieved magnitudes of rain frequency are lower than the climatological values at high latitudes. Results also show agreements in magnitude and temporal variation of monthly rainfall to atoll rain gauge measurements. They are consistent with other PIP-3 algorithms. The comparisons of zonally averaged monthly rainfall derived from SSM/I and the climatological datasets show that they are similar except for high latitudes where the retrieved values are biased low. This high-latitude low bias likely stems from the fact that the FSU algorithm does not retrieve accurately for dry snow conditions. Nevertheless, the consistencies in the comparisons motivate analysis of the distribution and magnitudes of latent heating over large expanses of the ocean basins between 40°S and 40°N.

The horizontal distribution of monthly mean latent heating shows that large heating centers lie in the vicinity and along the axes of well-documented large-scale convergence areas, consistent with the distribution of maximum monthly rainfall. The distribution of vertically averaged monthly latent heating shows a maximum heating rate of ~1.75°C day^{-1} in the west Pacific warm pool area in winter. The temporal variations of these heating centers clearly represent the variations of large-scale climate–weather systems. In addition, the results exhibit the varying properties of seasonal variations and subseasonal structures of latent heating over different regimes of the global oceans. The most significant feature in this regard is the summer Indian monsoon development and its intraseasonal oscillation.

The vertical distribution of monthly mean latent heating shows that maximum heating rates of ~5°C day^{-1} are located near the 5-km height level, with positive heating extending to the top of the troposphere in the Tropics. Additional relatively large heating rates are found around the 1-km height level. The heating magnitudes are consistent with results from Schaack et al. (1990) and Schaack and Johnson (1994). The longitude–height distributions of heating over the equatorial area show that large heating rates exist over the entire Pacific region with the maximum lying in the central Pacific area during the 1992 ENSO episode, then shifting to the west Pacific area with a smaller heating rate in the east Pacific area after May. These features document how the rising branch of the Walker circulation located in the west Pacific region during normal conditions, shifting to the central Pacific area during the 1992 ENSO episode, influences the position and magnitude of the main tropical diabatic heating center.

The comparisons of monthly rainfall and rain fre-

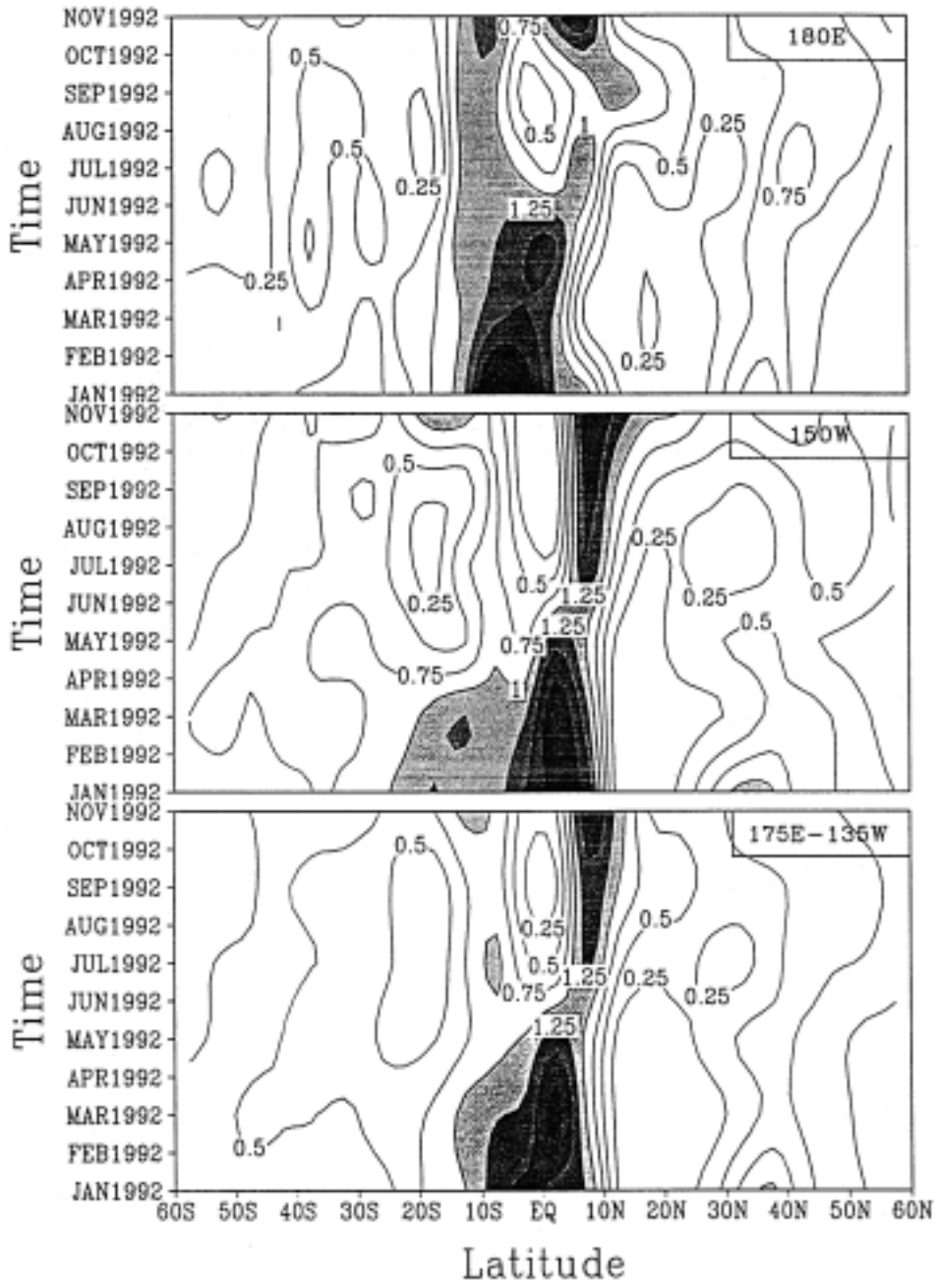

FIG. 12. Time–latitude sections of vertically averaged monthly latent heating for selected regions of SPCZ: (top), (middle), and (bottom) for 180°, 150°W, and 175°E–135°W. Contour interval is 0.25°C day^{-1} with shading for heating more than 1.0°C day^{-1}.

quency distributions suggest that the disturbances over the SPCZ are transient waves. The heating field associated with the SPCZ is further investigated to determine the response of the heating to the SPCZ system. The time–latitude sections of vertically averaged latent heating anomaly at the date line (zonal portion of SPCZ) and at the 150°W meridian (diagonal portion of SPCZ) show that the SPCZ becomes intensified in the Northern Hemisphere winter and weakened in summer. The time–longitude section of the vertically averaged latent heating anomaly over the equator–15°S zone shows that disturbances intensify once they are in the east Indian Ocean and central-east Pacific areas. The disturbances are out of phase over the Indian and central Pacific Oceans, while in phase over the Indian and east Pacific Oceans. These kinds of phase relationships between the disturbances suggest the occurrence of transient waves. These waves propagate eastward rapidly during the tran-

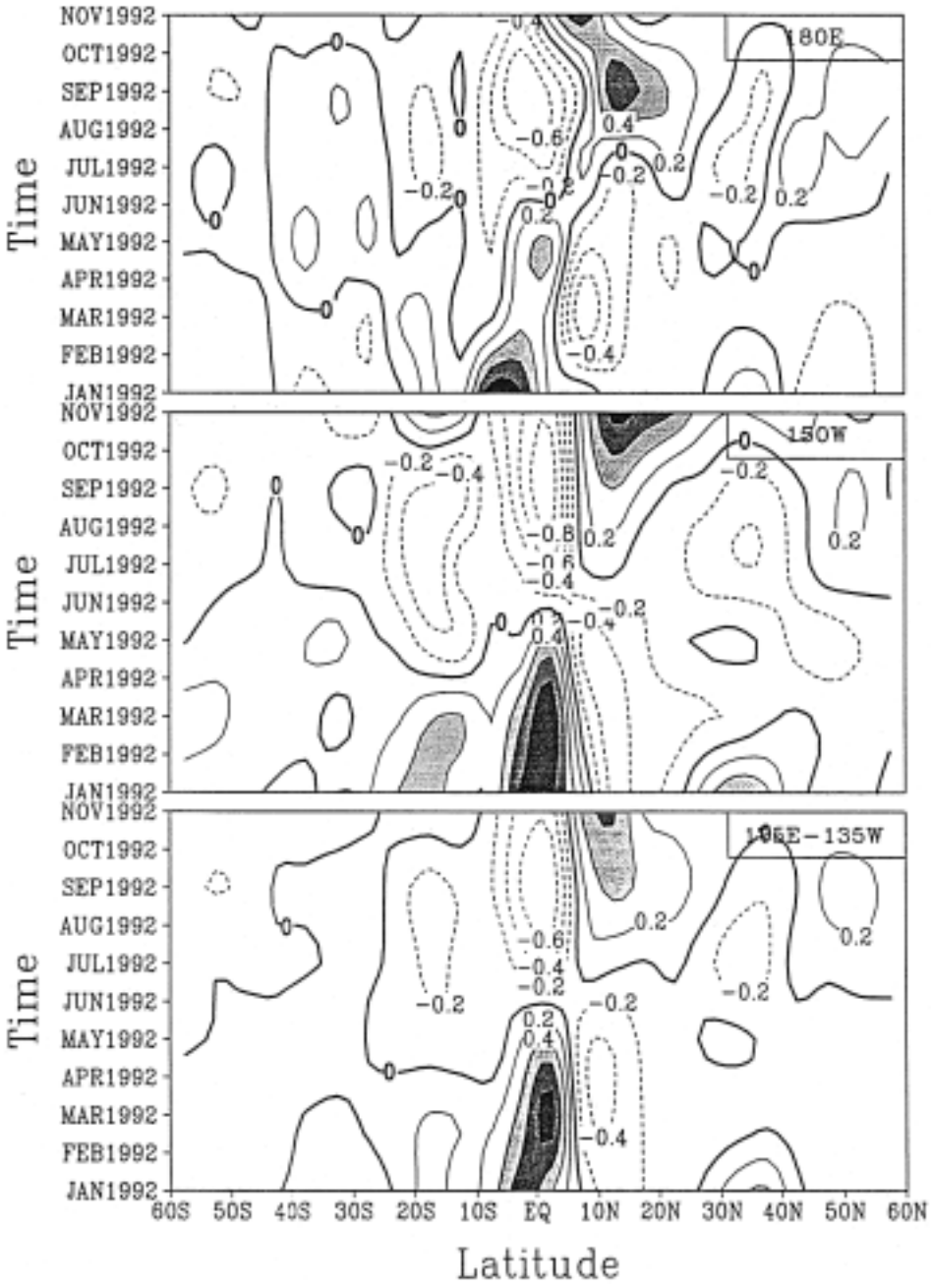

FIG. 13. Same as Fig. 12 except for departure of vertically averaged monthly latent heating. Contour interval is 0.2°C day^{-1} with shading for heating anomalies more than 0.4°C day^{-1} (bold line is zero; dashed lines are negative).

sient period between seasons, while moving slowly within seasons. This feature is an important characteristic of the seasonal variation of the SPCZ.

Although there are no real-time measured monthly surface rainfall and latent heating datasets to validate the results from this study, the general agreement between retrieved monthly rainfall and climatological data and the consistency between space–time variations of retrieved latent heating to documented climate behavior provide motivation for retrieving monthly three-dimensional rainfall and latent heating structures over global tropical–subtropical ocean areas. The seasonal variations of rainfall and latent heating are clearly depicted in the retrievals. Intraseasonal oscillations are detectable although they cannot be described in full detail with monthly datasets. Therefore, retrievals of daily rainfall and latent heating are under way to investigate detailed intraseasonal signals in the heating field in order to bet-

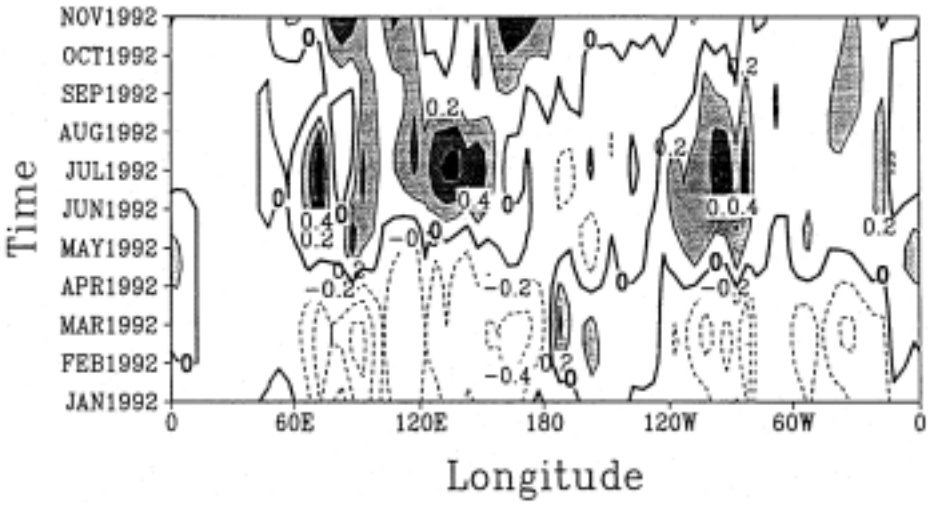

FIG. 14. Time–longitude section of departure of vertically averaged monthly latent heating for equator–15°S. Contour interval is 0.2°C day^{-1} with shading for heating anomalies more than 0.2°C day^{-1} (bold line is zero; dashed lines are negative).

ter understand the connections between the ITCZ, SPCZ, and monsoon systems.

It is not straightforward to validate the vertical structure of latent heating retrieved from SSM/I measurements. This is because the only practical type of comparison data based on conventional sounding measurements is the total moistening term Q_2, which is not equivalent to latent heating since it contains the vertical divergence of eddy moisture flux. However, results from this study in comparison to previous studies identified in section 4 have demonstrated that the vertical integrals of retrieved latent heating are consistent, while the comparisons concerning the vertical profiles are qualitatively encouraging. Although we do not have any confirming data with which to quantitatively assess the uncertainties in the vertical profiles, further improvements in retrieving the latent heating structure can be obtained by combining overflying radar measurements with passive microwave measurements since radar measurements provide additional detail on cloud vertical structure. Such combined algorithm approaches are under way within the TRMM project, which should be able to advance our understanding of the stationary and transient behavior of diabatic heating.

Acknowledgments. The authors wish to thank Mr. Jim Merritt for his capable assistance in processing the SSM/I and ECMWF datasets. This research has been supported by National Science Foundation Grant ATM-9300870 and National Aeronautics and Space Administration Grant NAG-52672. A portion of the computing resources has been provided by the Supercomputer Computation Research Institute at The Florida State University under U.S. Department of Energy Contract DOE-FC05-85ER250000.

APPENDIX

Description of the FSU Precipitation Profile Retrieval Algorithm

The FSU precipitation profile retrieval algorithm is based on the concept that an explicit three-dimensional cloud model can be used to provide the microphysical underpinnings for an inversion-based retrieval procedure. The algorithm is a physical inversion technique designed to accept any combination of polarized or unpolarized satellite or aircraft PMW measurements. The algorithm is based on a multispectral radiative inversion-optimization technique for a media containing scattering constituents. It is designed to retrieve the hydrometeor profiles of cloud, rain, as well as precipitating and nonprecipitating ice. The theoretical background for the algorithm has been discussed in the studies of Mugnai and Smith (1988), Smith and Mugnai (1988, 1989), Mugnai et al. (1990), Smith et al. (1992a), and Mugnai et al. (1993). The actual design of the algorithm for satellite applications has been described by Smith et al. (1994a,b), and for aircraft applications by Smith et al. (1994d) and Marzano et al. (1994). Smith et al. (1994c) also provided an overview of the conceptual and theoretical issues behind profile-type precipitation retrieval algorithms.

The FSU retrieval algorithm configured for SSM/I measurements consists of three key components: 1) a set of cloud-radiation model calculations forming an initial guess database; 2) spatially deconvolved or convolved SSM/I measurements at 19, 22, 37, and 85 GHz; and 3) a radiative transfer equation (RTE) model configured as a functional to an optimization scheme. The initial cloud microphysics used in the algorithm are based on output from a three-dimensional, fully nested–

full physics, nonhydrostatic mesoscale model, run in a design in which the inner nest grid mesh is set at a cloud-resolving scale. This model, referred to as the University of Wisconsin Nonhydrostatic Modeling System, was developed and has been described by Tripoli (1992a,b). The microphysical equations in the model carry terms for cloud drops, raindrops, graupel particles, pristine ice crystals, snowflakes, and ice aggregates. Thousands of distinct microphysical profiles derived from the cloud model are used as input to the RTE model providing the initial guess database of microphysical profiles coupled with their radiative signatures given as upwelling brightness temperatures (T_B's) at the top of atmosphere at the preferred microwave frequencies and polarizations.

The RTE model consists of a two-stream solution to the azimuthally independent radiative transfer equation, allowing for arbitrary surface boundary conditions, and unfolding of the zenith-dependent radiance field for match up to the actual radiometer look angle. The RTE model is adapted from the two-stream delta-Sobolev model developed by Xiang et al. (1994) for solar applications, with its passive microwave counterpart being described in Smith et al. (1994a).

Sea surface temperature and temperature–moisture profile data required for input to the RTE model are chosen from either available measurements, prognostic products, or climatologies.

For a small study area, the deconvolution approach is preferable. To initiate the retrieval process, calibrated SSM/I T_B's at 19, 22, and 37 GHz are spatially enhanced to the resolution of the 85-GHz channels such that there is footprint conformity for all channels. This is based on the energy-conserving spatial deconvolution scheme for SSM/I applications developed by Farrar and Smith (1992). Its impact on precipitation retrieval and its ability to partially offset problems due to nonhomogeneous beam filling has been described by Farrar et al. (1994). As shown in the latter paper, the need for a beam filling adjustment factor is not absolutely crucial for this type of algorithm since it uses information at both emission and scattering frequencies; however, applying the deconvolution operator provides better physical consistency with the RTE calculations.

Given the measured multispectral T_B's at pixel coordinates, a selection process is applied to obtain initial guess profiles from the database needed by the RTE model for carrying out the inversion process. This involves applying the RTE model in a forward perturbative mode until the 19-, 37-, and 85-GHz channels averaged rms between the modeled and measured T_B's is less than 0.1 K. The perturbation process is guided by a numerical optimization scheme [the golden search method described in Gill et al. (1981)], which generates a unique solution profile from a set of initial guess profiles. On average, the inversion procedure improves upon the initial guess by approximately 30% using a normalized error function as the metric, although for individual cases improvements can range from small (~0%) to large (>100%). A detailed description of the selection–optimization procedures can be found in Smith et al. (1994a).

The algorithm estimates vertical profiles of liquid and ice water contents, that is, LWC(z), IWC(z), for precipitating raindrops and ice particles, as well as LWCs and IWCs for suspended cloud drops and ice particles. The vertical rain rate and mass flux profiles, as well as surface rain rates, are derived from a gravity fallout equation consistent with that applied in the cloud model. The vertical rain rate profiles $\mathrm{RR}_{\mathrm{rd}}(z)$ are given by

$$\mathrm{RR}_{\mathrm{rd}}(z) = -\rho_o(z)\left[\overline{W}_{\mathrm{rd}}(z) + \overline{W}(z)\right]q_{\mathrm{rd}}(z)/\rho_w, \quad \text{(A1)}$$

where ρ_o is the basic state air density, ρ_w the water density (1000 kg m^{-3}), q_{rd} the rainwater mixing ratio, $\overline{W}(z)$ the cloud-scale vertical velocity, and $\overline{W}_{\mathrm{rd}}(z)$ the vertically dependent mean terminal velocity, where

$$\overline{W}_{\mathrm{rd}}(z) = -1.94\left[\frac{4\rho_w D_{m_w} g}{3C_{D_w}\rho_o(z)}\right]^{1/2} \quad \text{(A2)}$$

and g, C_{D_w}, and D_{m_w} are the gravitational acceleration, the water drop drag coefficient (0.588), and the characteristic diameter of the raindrops (540 μm). The terms on the right-hand side are given in SI units whereas $\mathrm{RR}_{\mathrm{rd}}$ is in millemeters per second. Applying Eq. (A1) at the surface level leads to the surface rain rate.

A similar expression for ice particles is given by

$$\mathrm{RR}_{\mathrm{ip}}(z) = -\rho_o(z)\left[\overline{W}_{\mathrm{ip}}(z) + \overline{W}(z)\right][q_{\mathrm{ip}}(z)/\rho_i], \quad \text{(A3)}$$

where

$$\overline{W}_{\mathrm{ip}}(z) = -\left[\frac{4\rho_i D_{m_i} g}{3C_{D_i}\rho_o(z)}\right]^{1/2} \quad \text{(A4)}$$

with ice particle drag coefficient, density, and characteristic diameter chosen as 0.45, 600 kg m^{-3}, and 1000 μm, respectively.

Various modifications to the original version of the FSU algorithm have been implemented by Yang and Smith (1999), including 1) an improved surface emissivity model that includes the effects of a wind roughened sea surface roughness and wind-generated foam, 2) accounting for the effects of nonprecipitating cloud hydrometeors under vertical motion on the latent heating profile, and 3) including the effects of cloud-scale vertical velocity on diagnosed rain and heating rates. In addition, a new screening scheme was developed to distinguish between clear, cloud without rain, and cloud with rain SSM/I pixels to better depict the vertical structure of heating. The cloud-scale vertical velocity ($\overline{W}$) is estimated through a regression method using the retrieved hydrometeor profiles of cloud, raindrops, graupel particles, ice crystals, and snowflakes. The regression equation is

$$\overline{W}_i = A_i + B_i\mathrm{Cloud}_i + C_i\mathrm{Rain}_i + D_i\mathrm{Graupel}_i + E_i\mathrm{Ice}_i + F_i\mathrm{Snow}_i, \quad \text{(A5)}$$

where $\overline{W}$ is the regressed vertical velocity, A, B, . . . , and F are the regression coefficients, and the subscript i is the model level. The complete form of surface emissivity is given by

$$\varepsilon = (\varepsilon_s - \Delta\varepsilon_r)(1 - f_c) + \varepsilon_f f_c, \qquad \text{(A6)}$$

where ε is the surface emissivity, ε_s the specular emissivity, $\Delta\varepsilon_r$ the correction of emissivity due to surface roughness, ε_f the emissivity of foam, and f_c the foam coverage.

Validation of the retrieved rainrates was conducted in the AIP-3 study area, relative to a set of shipboard C-band radar measurements described by Short et al. (1997). In this analysis, the intercomparisons of daily mean rain rate and rain-area coverage from SSM/I and radar measurements over the TOGA COARE IOP show that the overall bias and correlation coefficient are 0.013 mm h^{-1} and 0.746 for daily rain rate, and 1.9% and 0.857 for rain-area coverage, respectively; see Yang and Smith (1999). This study also considered validations at instantaneous and monthly timescales.

Latent heating profiles are obtained by evaluating the vertical derivative of retrieved liquid–ice water mass fluxes, which are proportional to condensation and deposition heating fluxes along the height axis. The mass flux profiles for cloud drops (R^*_{cd}), precipitating raindrops (R^*_{rd}), and precipitating ice particles (R^*_{ip}) are given by

$$R^*_{cd}(z) = -\overline{W}(z)\mathrm{LWC}_{cd}(z) \qquad \text{(A7)}$$

$$R^*_{rd}(z) = -\left[\overline{W}_{rd}(z) + \overline{W}(z)\right]\mathrm{LWC}_{rd}(z) \qquad \text{(A8)}$$

$$R^*_{ip}(z) = -\left[\overline{W}_{ip}(z) + \overline{W}(z)\right]\mathrm{IWC}_{ip}(z), \qquad \text{(A9)}$$

where LWC_{cd}, LWC_{rd}, and IWC_{ip} (retrieved in units of g m^{-3}) are the liquid and ice water contents for cloud drops, raindrops, and ice particles, respectively. Here, $\overline{W}_{rd}$ and $\overline{W}_{ip}$ are the vertically dependent mean terminal velocities (m s^{-1}) for raindrops and ice particles.

Therefore, total latent heating due to the combination of ascending or descending cloud drops, raindrops, and graupel particles is given by the sum of the vertical derivatives of the mass fluxes:

$$Q(z) = \frac{g}{c_p}\left\{L_v\left[\frac{\partial R^*_{cd}(z)}{\partial p}\right] + L_v\left[\frac{\partial R^*_{rd}(z)}{\partial p}\right] + (L_v + L_f)\left[\frac{\partial R^*_{ip}(z)}{\partial p}\right]\right\}, \qquad \text{(A10)}$$

where L_v/L_f are the latent heats of vaporization/fusion and c_p is isobaric specific heat.

Because of the nature of inversion-based physical retrieval, the computational barriers are formidable for global-scale retrievals at pixel resolution. An alternative strategy, which was used in this study, was implemented for overcoming the computational problem. The basic approach is to generate a database in which the hydrometeor profiles and surface rain-rate relationships corresponding to unpolarized T_B's along 19-, 37-, and 85-GHz axes are gridded at 5°C brightness temperature resolution. The temperature–moisture profiles and SSTs needed for input to the RTE model are based on monthly averaged data from European Centre for Medium-Range Weather Forecasts datasets at a $10° \times 10°$ grid resolution. This database is generated for each month and for each 10° of latitude–longitude.

The databases are then used as a lookup table solution in which six parameters are involved to obtain an unique solution for a given measurement vector at 19, 37, and 85 GHz. The six parameters represent the three T_B axes, the month axis, and the latitude–longitude axes. The last three variables determine which T_B look-up table will be used. Three measured T_B's are then used in an interpolation process. The grid size of a table is $30 \times 25 \times 27$, in which the 19-GHz axis extends from 135 to 285 K, the 37-GHz axis from 160 to 285 K, and the 85-GHz axis from 150 to 285 K. A modified version of the Ferraro et al. (1996) rain-rate screen is used to detect raining pixels.

A comparison of the pixel-based solution against the lookup table solution for a test dataset taken over the AIP-3 study area indicates that monthly rainfall from the lookup table solution is ~13% larger. However, this bias has zero impact on the heating calculations as we have forced the heating bias to zero relative to rainfall measurements taken by TOGA COARE ship radars as indicated in section 2. Furthermore, even without constraining the heating bias, a small bias in retrieved rainfall would have minor influence on retrieved heating rates since they represent vertical derivatives of rain mass fluxes.

REFERENCES

Adler, R. F., G. J. Huffman., and P. R. Keehn, 1994: Global tropical rain estimates from microwave-adjusted geosynchronous IR data. *Remote Sens. Rev.*, **11,** 125–152.

——, C. Kidd, M. Goodman, A. Ritchie, R. Schudalla, G. Petty, M. Morrissey, and S. Greene, 1996: PIP-3 intercomparison results. *PIP-3 Workshop.* [Available from R. Adler, NASA/Goddard Space Flight Center, Greenbelt, MD 20771.]

Arkin, P. A., and P. Xie, 1994: The Global Precipitation Climatology Project: First Algorithm Intercomparison Project. *Bull. Amer. Meteor. Soc.*, **75,** 401–419.

Bell, G. D., and A. N. Basist, 1994: The global climate of December 1992–February 1993. Part I: Warm ENSO conditions continue in the tropical Pacific; California drought abates. *J. Climate,* **7,** 1581–1605.

Chang, S. W., and T. R. Holt, 1994: Impact of assimilating SSM/I rainfall rates on numerical prediction of winter cyclones. *Mon. Wea. Rev.,* **122,** 151–164.

Chen, T.-C., and W. E. Baker, 1986: Global diabatic heating during FGGE SOP-1 and SOP-2. *Mon. Wea. Rev.*, **114,** 2578–2589.

Farrar, M. R., and E. A. Smith, 1992: Spatial resolution enhancement of terrestrial features using deconvolved SSM/I microwave brightness temperatures. *IEEE Trans. Geosci. Remote Sens.*, **30,** 349–355.

——, ——, and X. Xiang, 1994: The impact of spatial resolution enhancement of SSM/I microwave brightness temperatures on rainfall retrieval algorithms. *J. Appl. Meteor.*, **33,** 313–333.

Ferraro, R. R., F. Weng, N. C. Grody, and A. Basist, 1996: An eight-year (1987–1994) time series of rainfall, clouds, water vapor,

snow cover, and sea ice derived from SSM/I measurements. *Bull. Amer. Meteor. Soc.,* **77,** 891–905.
Gill, P. E., W. Murray, and M. H. Wright, 1981: *Practical Optimization.* Academic Press, 401 pp.
Hack, J. J., and W. H. Schubert, 1990: Some dynamical properties of idealized thermally-forced meridional circulations in the tropics. *Meteor. Atmos. Phys.,* **44,** 101–118.
Hartmann, D. L., H. H. Hendon, and R. A. Houze Jr., 1984: Some implications of the mesoscale circulations in tropical cloud cluster for large-scale dynamics and climate. *J. Atmos. Sci.,* **41,** 113–121.
Holopainen, E., and C. Fortelius, 1986: Accuracy of estimates of atmospheric large-scale energy flux divergence. *Mon. Wea. Rev.,* **114,** 1910–1921.
Huffman, G. F., R. F. Adler, B. Rudolf, U. Scheider, and P. Keehn, 1995: Global precipitation estimates based on a technique for combining satellite-based estimates, rain gauge analysis, and NWP model precipitation information. *J. Climate,* **8,** 1284–1295.
Jaeger, L., 1983: Monthly and areal patterns of mean global precipitation. *Variations in the Global Water Budget,* D. Reidel, 129 pp.
Janowiak, J. E., 1992: Tropical rainfall: A comparison of satellite-derived rainfall estimates with model precipitation forecasts, climatologies, and observations. *Mon. Wea. Rev.,* **120,** 448–462.
——, 1993: The global climate for September–November 1991: Warm (ENSO) episode conditions strengthen. *J. Climate,* **6,** 1616–1638.
Kousky, V. E., 1993: The global climate of December 1991–February 1992: Mature phase warm (ENSO) episode conditions develop. *J. Climate,* **6,** 1639–1655.
Krishnamurti, T. N., H. S. Bedi, and K. Ingles, 1993: Physical initialization using SSM/I rain rates. *Tellus,* **45A,** 247–269.
——, G. D. Rohaly, and H. S. Bedi, 1994: On the improvement of precipitation forecast skill from physical initialization. *Tellus,* **46A,** 598–614.
Kummerow, C., and L. Giglio, 1994a: A passive microwave technique for estimating rainfall and vertical structure information from space. Part I: Algorithm description. *J. Appl. Meteor.,* **33,** 3–18.
——, and ——, 1994b: A passive microwave technique for estimating rainfall and vertical structure information from space. Part II: Applications to SSM/I data. *J. Appl. Meteor.,* **33,** 19–34.
——, W. S. Olson, and L. Giglio, 1996: A simplified scheme for obtaining precipitation and vertical hydrometeor profiles from passive microwave sensors. *IEEE Trans. Geosci. Remote Sens.,* **34,** 1213–1232.
Lau, K. M., and P. H. Chen, 1985: Aspects of the 40–50 day oscillation during the northern summer as inferred from outgoing longwave radiation. *Mon. Wea. Rev.,* **113,** 1889–1909.
——, and L. Peng, 1987: Origin of low-frequency (intraseasonal) oscillations in the tropical atmosphere. Part I: The basic theory. *J. Atmos. Sci.,* **44,** 950–972.
Legates, D. G., and C. J. Wilmott, 1990: Mean seasonal and spatial variability in gauge-corrected, global precipitation. *Int. J. Climatol.,* **10,** 111–127.
Marzano, F., A. Mugnai, E. A. Smith, X. Xiang, J. E. Turk, and J. Vivekanandan, 1994: Active and passive remote sensing of precipitating storms during CaPE. Part II: Intercomparison of precipitation retrievals from AMPR radiometer and CP-2 radar. *Meteor. Atmos. Phys.,* **54,** 29–51.
Meehl, G. A., 1987: The annual cycle and interannual variability in the tropical Pacific and Indian Ocean regions. *Mon. Wea. Rev.,* **115,** 27–50.
Mo, K., and X. Wang, 1994: The global climate of June 1992–August 1992: Warm ENSO episode decays and colder than normal conditions dominate the Northern Hemisphere. *J. Climate,* **7,** 335–357.
Mugnai, A., and E. A. Smith, 1988: Radiative transfer to space through a precipitating cloud at multiple microwave frequencies. Part I: Model description. *J. Appl. Meteor.,* **27,** 1055–1073.
——, H. J. Cooper, E. A. Smith, and G. J. Tripoli, 1990: Simulation of microwave brightness temperatures of an evolving hail storm at SSM/I frequencies. *Bull. Amer. Meteor. Soc.,* **71,** 2–13.
——, E. A. Smith, and G. J. Tripoli, 1993: Foundations for statistical–physical precipitation retrieval from passive microwave satellite measurements. Part II: Emission-source and generalized weighting-function properties of a time-dependent cloud-radiation model. *J. Appl. Meteor.,* **32,** 17–39.
Petty, G. W., 1995: Frequencies and characteristics of global oceanic precipitation from shipboard present-weather reports. *Bull. Amer. Meteor. Soc.,* **76,** 1593–1616.
Puri, K., and N. E. Davidson, 1992: The use of infrared satellite cloud imagery data as proxy data for moisture and diabatic heating in data assimilation. *Mon. Wea. Rev.,* **120,** 2329–2341.
Rasmusson, E. M., and T. H. Carpenter, 1982: Variations in tropical sea surface temperature and surface wind fields associated with the Southern Oscillation/El Niño. *Mon. Wea. Rev.,* **110,** 354–384.
——, and P. A. Arkin, 1993: A global view of large-scale precipitation variability. *J. Climate,* **6,** 1495–1522.
Raymond, W. H., W. S. Olson, and G. Callan, 1995: Diabatic forcing and initialization with assimilation of cloud water and rainwater in a forecast model. *Mon. Wea. Rev.,* **123,** 366–382.
Ropelewski, C. F., and M. S. Halpert, 1987: Global and regional scale precipitation patterns associated with the El Niño/Southern Oscillation. *Mon. Wea. Rev.,* **115,** 1606–1626.
Schaack, T. K., and D. R. Johnson, 1994: January and July global distributions of atmospheric heating for 1986, 1987, and 1988. *J. Climate,* **7,** 1270–1285.
——, ——, and M.-Y. Wei, 1990: The three-dimensional distribution of atmospheric heating during the GWE. *Tellus,* **42A,** 305–327.
Schneider, U., and B. Rudolf, 1994: Differences between 1987 and 1988 summer monsoon rainfall over India, Southeast Asia and the Indian Ocean as obtained from the preliminary GPCP merged global data set. *Proc. Int. Conf. on Monsoon Variability and Prediction,* Trieste, Italy, Italian National Research Council.
Shinoda, T., and R. Lukas, 1995: Lagrangian mixed layer modeling of the western equatorial Pacific. *J. Geophys. Res.,* **100,** 2523–2541.
Short, D. A., P. A. Kucera, B. S. Ferrier, J. C. Gerlach, S. A. Rutledge, and O. W. Thiele, 1997: Shipboard radar rainfall patterns within the TOGA COARE IFA. *Bull. Amer. Meteor. Soc.,* **78,** 2817–2836.
Sikka, D. R., and S. Gadgil, 1980: On the maximum cloud zone and the ITCZ over Indian longitudes during the southwest monsoon. *Mon. Wea. Rev.,* **108,** 1840–1853.
Simpson, J., C. Kummerow, W.-K. Tao, and R. F. Adler, 1996: On the Tropical Rainfall Measuring Mission (TRMM). *Meteor. Atmos. Phys.,* **60,** 19–36.
Smith, E. A., and A. Mugnai, 1988: Radiative transfer to space through a precipitating cloud at multiple microwave frequencies. Part II: Results and analysis. *J. Appl. Meteor.,* **27,** 1074–1091.
——, and ——, 1989: Radiative transfer to space through a precipitating cloud at multiple microwave frequencies. Part III: Influence of large ice particles. *J. Meteor. Soc. Japan,* **67,** 739–755.
——, ——, H. J. Cooper, G. J. Tripoli, and X. Xiang, 1992a: Foundations for statistical–physical precipitation retrieval from passive microwave satellite measurements. Part I: Brightness-temperature properties of a time-dependent cloud-radiation model. *J. Appl. Meteor.,* **31,** 506–531.
——, X. Xiang, A. Mugnai, and G. Tripoli, 1992b: A cloud radiation model for spaceborne precipitation retrieval. *Extended Abstracts, Int. TRMM Workshop on the Processing and Utilization of the Rainfall Data Measured from Space,* Tokyo, Japan, Communications Research Laboratory, 273–283.
——, ——, ——, and ——, 1994a: Design of an inversion-based precipitation profile retrieval algorithm using an explicit cloud model for initial guess microphysics. *Meteor. Atmos. Phys.,* **54,** 53–78.
——, A. Mugnai, and G. Tripoli, 1994b: Theoretical foundations and verification of a multispectral, inversion-type microwave pre-

cipitation profile retrieval algorithm. *Proceedings of the ESA/NASA International Workshop on Microwave Radiometry*, B. J. Choudhury, Y. H. Kerr, E. G. Njoku, and P. Pampaloni, Eds., VSP Science Press, 599–621.

——, C. Kummerow, and A. Mugnai, 1994c: The emergence of inversion-type precipitation profile algorithms for estimation of precipitation from satellite microwave measurements. *Remote Sens. Rev.*, **11,** 211–242.

——, X. Xiang, A. Mugnai, R. Hood, and R. W. Spencer, 1994d: Behavior of an inversion-based precipitation retrieval algorithm with high resolution AMPR measurements including a low frequency 10.7 GHz channel. *J. Atmos. Oceanic Technol.*, **11,** 858–873.

——, and Coauthors, 1998: Results of WetNet PIP-2 project. *J. Atmos. Sci.*, **55,** 1483–1536.

Spencer, R. W., 1993: Global oceanic precipitation from the MSU during 1979–1991 and comparisons to other climatologies. *J. Climate*, **6,** 1301–1326.

Tao, W.-K., J. Simpson, S. Lang, M. McCumber, R. Adler, and R. Penc, 1990: An algorithm to estimate the heating budget from vertical hydrometeor profiles. *J. Appl. Meteor.*, **29,** 1232–1244.

——, S. Long, J. Simpson, and R. Adler, 1993: Retrieval algorithms for estimating the vertical profiles of latent heat release: Their applications for TRMM. *J. Meteor. Soc. Japan*, **71,** 685–700.

Trenberth, K. E., 1983: Interactions between orographically and thermally forced planetary waves. *J. Atmos. Sci.*, **40,** 1126–1152.

Tripoli, G. J., 1992a: A nonhydrostatic model designed to simulate scale interaction. *Mon. Wea. Rev.*, **120,** 1342–1359.

——, 1992b: An explicit three-dimensional nonhydrostatic numerical simulation of a tropical cyclone. *Meteor. Atmos. Phys.*, **49,** 229–254.

Vincent, D. G., 1994: The Southern Pacific Convergence Zone (SPCZ): A review. *Mon. Wea. Rev.*, **122,** 1949–1970.

Wang, X., 1993: The global climate of March–May 1992: Mature phase warm episode continues in the tropical Pacific. *J. Climate*, **6,** 2465–2485.

Webster, P. J., 1983: The large scale structure of the tropical atmosphere. *General Circulation of the Atmosphere*, B. M. Hoskins and R. Pearce, Eds., Academic Press, 235–275.

——, and H. R. Chang, 1988: Equatorial energy accumulation and emanation region: Impacts of a zonally varying basic state. *J. Atmos. Sci.*, **45,** 803–829.

Wei, M.-Y., D. R. Johnson, and R. D. Townsend, 1983: Seasonal distributions of diabatic heating during First GARP Global Experiment. *Tellus*, **35A,** 241–255.

Wilheit, T., and Coauthors, 1994: Algorithms for the retrieval of rainfall from passive microwave measurements. *Remote Sens. Rev.*, **11,** 163–194.

Xiang, X., E. A. Smith, and C. G. Justus, 1994: A rapid radiative transfer model for reflection of solar radiation. *J. Atmos. Sci.*, **51,** 1978–1988.

Yanai, M., and T. Tomita, 1998: Seasonal and interannual variability of atmospheric heat sources and moisture sinks as determined from NCEP–NCAR reanalysis. *J. Climate*, **11,** 463–482.

——, S. Esbensen, and J. H. Chu, 1973: Determination of bulk properties of tropical cloud clusters from large-scale heat and moisture budgets. *J. Atmos. Sci.*, **30,** 611–627.

Yang, S., and E. Smith, 1999: Moisture budget analysis of TOGA COARE area using SSM/I-retrieved latent heating and large scale Q_2 estimates. *J. Atmos. Oceanic Technol.*, in press.

Yasunari, T., 1979: Cloudiness fluctuations associated with the Northern Hemisphere summer monsoon. *J. Meteor. Soc. Japan*, **57,** 227–242.